Multiscale Optoelectronic Properties of Nanostructured Zinc Oxide Ultraviolet Photodetectors

By

Brent K. Cook

Submitted to the Department of Physics and Astronomy and the Graduate Faculty of the University of Kansas in partial fulfillment of the requirements for the degree of Master of Science.

_____

Chairperson Dr. Judy Wu

_____

Dr. Hui Zhao

_____

Dr. Wai-Lun Chan

Date Defended: 5 May 2017

The Thesis Committee for Brent K. Cook
certifies that this is the approved version of the following thesis:

Multiscale Properties of Nanostructured Zinc Oxide Ultraviolet Photodetectors

_____

Chairperson Dr. Judy Wu

Date approved: 5 May 2017

Abstract

Zinc oxide nanostructures, such as ZnO nanowires (NWs) and quantum dots (QDs) were fabricated via solution routes and incorporated with graphene to form high-performance ZnO/graphene nanohybrid ultraviolet optoelectronic devices. Structures such as vertically aligned ZnO-NWs/graphene heterojunction nanohybrids combine the superior sensitivity of crystalline ZnO-NWs with high charge mobility of graphene, allowing high device performance surpassing their conventional counterparts'. Controlling the ZnO nanostructure morphology and its interface with graphene is important to optimization of the optoelectronic processes including exciton dissociation, charge transfer and transport, which in turn affects the ZnO/graphene nanohybrids device performance. This thesis explored two types of ZnO/graphene nanohybrids: one with vertically aligned ZnO-NWs grown directly on graphene and the other, with porous ZnO printed on graphene. In the former, we have found that a ZnO seed layer facilitates growth of a dense array ZnO-NWs of radii approaching the Debye length (~20 nm) that is desired for optimal surface electron depletion effect. In contrast, a seedless process resulted in a lower density of ZnO-NWs of a larger diameter on the order of sub-to-few micrometers. Consequently, higher UV photoresponsivity up to 728 A/W was obtained on ZnO-NW/graphene nanohybrids obtained in the seeded process, which is anticipated from the larger surface-to-volume ratio and hence more enhanced photoconductive gain from the surface electron depletion. However, a strong charge trapping effect was also introduced by the seed layer at the ZnO-NW/graphene interface, leading to much slower photoresponse. In the printed ZnO nanohybrids, inks of zinc acetate precursor without (ZnOPr) and with crystalline ZnO QDs (ZnOPrQDs) have been explored. The former exhibited a micro-porous structure while the latter, nanoporous with feature size comparable to the ZnO's Debye length. Without graphene, higher UV photoresponsivity of 383.6 A/W and the on/off

ratio of 2470 were observed in nanoporous ZnO photoconductors as expected, which are significantly better than that of 14.7 A/W and 949 in the microporous counterparts. With graphene, the ZnO/graphene exhibited a photoresponse of ~1000 A/W and a photoconductive gain of 1.8×10^4, a whole order of magnitude better than without graphene. These nanostructures have demonstrated high performances and printability for sensor applications.

Acknowledgments

I would like to thank my advisor Dr. Judy Wu and collaborator Dr. Qingfeng Liu for all the opportunities and help.

Table of Contents

List of Figures

Chapter 1

Zinc Oxide Ultraviolet Photodetector

1.1 *Ultraviolet Detection*

Modern electronics have witnessed constant decrease of transistor size described by empirical Moore's Law, resulting in a predictable trend in computing power during the last four decades [1]. A decrease in semiconductor device size down to the exciton Bohr radius [2, 3] of the electron-hole pairs (excitons), and the Debye length of the material [4-6], increases sensitivity of the semiconductor to surface effects. These surface effects can be problematic for some electronic devices, but advantageous for sensor technology. One type of sensor that is the focus for this work is the zinc oxide (ZnO) ultraviolet (UV) photodetector.

Ultraviolet light was first discovered in 1801 by J. W. Ritter and gained attention in 1950 – 1960's for rocket, space, and communication applications [7-9], and since expanded to a wide range of applications; such as, sterilization, monitoring pollution, communications, flame sensing, artillery, biosensing, and missile detection [9-12]. The ultraviolet electromagnetic spectrum ranges from 10-400 nm [13], and increasing attention to improving UV detectors in this wavelength range for performance and cost efficiency are continually pursued. UV detectors have been fabricated through phototubes, photomultiplier tubes, gas ion chambers and semiconductor devices, which are smaller and cheaper in fabrication [9, 14].

Ultraviolet detectors based on zinc oxide (ZnO) is the main focus for this work, as opposed to GaA, AlN, AlGaN, MgZnO, TiO_2, 4H-SiC, 6H-SiC, and diamond semiconductors, which operate in the UV range [15]. Properties of ZnO include excellent radiation hardness, a wide-direct

bandgap (3.4 eV), large exciton binding energy (60 meV) at room temperature, and versatile applications like piezoelectrics [16], gas sensing [17-19], biosensing [20, 21], and UV detection [15, 22]. ZnO can also be fabricated into many different nanostructures like flowers, hallow cages, quantum dots, thin films, nanowires, and various others structures [4, 23-25]. The types of morphologies/nanohybrids investigated with ZnO are nanowires hybridized with graphene via hydrothermal methods and ZnO quantum dots incorporated with ZnO precursor to form a nanocomposite film for UV detection.

1.2 *Energy Band Physics and Photodetector Characterization*

Conventional semiconductor UV detectors operate by absorption of photons that excite electrons in the bound state (valence energy band), E_V, of a semiconductor to the free-excited state (conduction band), E_C [26]. The energy difference of the conduction and valence energy bands is call the energy bandgap, E_g, of the semiconductor [26]. However, in a realistic situation there are usually some defects present in the crystal, which can introduce levels in the energy bandgap near the conduction band and/or valence band (Figure 1.2.1), these defects broaden the absorption spectrum of photons around the energy of the bandgap [26]. When the electrons are excited to the conduction energy band, they leave behind a hole, which carries a positive charge (Figure 1.2.1), and can result in an electron-hole pair to form, a bound state referred to as an exciton [26]. By energy conservation, to create an exciton the electron-hole pair must carry enough energy equivalent to the bandgap, binding, and kinetic energy. Excitons can be split apart by internal or external potential bias, or recombine to emit a photon [26]. Other exciton decay processes are also possible instead of photon emission, such as energy transfer to neighboring electrons, or energy lost in the form of heat [26].

The bandgap can be classified as either a direct bandgap or indirect bandgap. In a direct bandgap such as with ZnO, electrons have a direct path from the valence band to conduction band (Figure 1.2.1 a) and do not require a change in momentum, $\hbar\Delta k$, as seen in Figure 1.2.1 b, where $\hbar = \frac{h}{2\pi}$, and h is Plank's constant, 'k' is the wave number, and f is the photon frequency. For an indirect bandgap, the electrons are excited to the lowest energy state of the conduction band only through a change in momentum [26]. The change of momentum comes from interaction with phonons in the crystal, resulting in loss of momentum to the lattice so electrons and holes do not share the same momentum [26].

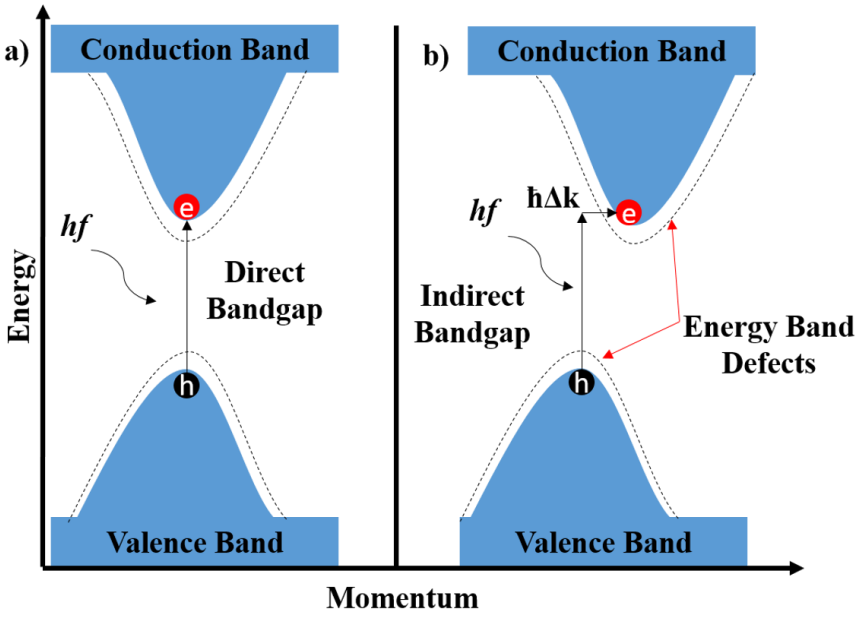

Figure 1.2.1 The electrons in the valence band (red dots) are excited to the conduction band and leave behind a hole (black dots). There are two kinds of bandgaps the (a) direct bandgap and (b) indirect bandgap.

As a direct bandgap semiconductor, ZnO allows for electrons a straight path to the lowest energy level in the conduction energy band, allowing efficient absorption of photons without

losing momentum to crystal interactions. Applying a voltage across the semiconductor causes electrons in the conduction band to flow through the semiconductor. The increased total current, I_{tot}, minus the current flow when the semiconductor is in the dark, I_{dark}, is called the photocurrent, $I_{ph} = I_{tot} - I_{dark}$ [27]. The photocurrent divided by the amount of optical power delivered, P_{in}, to the semiconductor is the photoresponsivity, $R = \frac{I_{ph}}{P_{in}}$, and the photocurrent divided by the dark current is the on-off ratio, $I_{ratio} = \frac{I_{ph}}{I_{dark}}$ [27]. The photoresponsivity can be used to calculate gain sometimes called external quantum efficiency, $G = R\frac{hf}{q}$, where h is Plank's constant and f is the photon frequency, and q is the elementary charge [27]. Alternatively, the gain can also be calculated by the transit time ($\tau_{transit}$) and life time (τ_{life}) of the charges and is given by $G = \frac{\tau_{life}}{\tau_{transit}}$ [27]. These quantities will play an important role in characterizing photodetectors and the differing performance between bulk and nanostructured devices.

1.3 *Metal-Semiconductor-Metal Photodetectors*

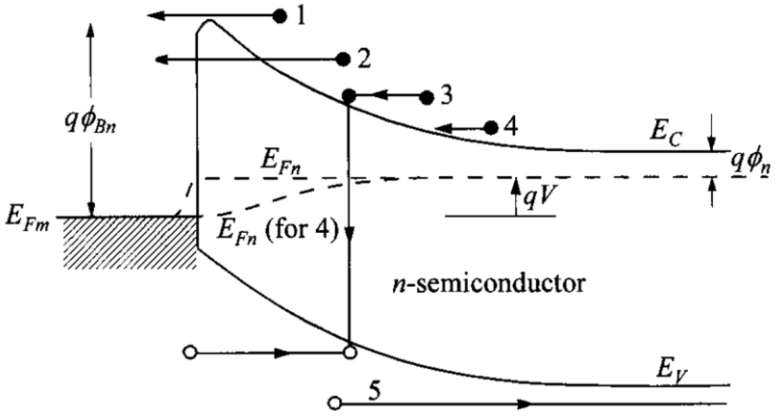

Figure 1.3.1 There are four process that contribute to charge transport across the energy barrier at metal-semiconductor interface; such as, (1) thermionic emission, (2) charge tunneling, (3) recombination, (4) electron diffusion, and (5) hole diffusion [26]. Adapted from *Physics of*

Semiconductor Devices (pg. 154), S. M. Sze and K. K. Ng, 2007, Hoboken, New Jersey John Wiley & Sons, Inc.

In Figure 1.3.1 depicts a general diagram for an n-type semiconductor in contact with a metal under a voltage bias *V*, where E_{Fm} and E_{Fn} are the fermi energies of the metal and n-type semiconductor respectively; E_C and E_V are the conduction bands and valence bands of the semiconductor; *q* is the charge, and ϕ_{Bn} is the potential barrier at the interface [26]. When the metal and semiconductor come into contact, there is an electric potential that forms from the charges at the surface of the semiconductor and the image charge on the metal [26]. The electric potential results in charge migration between metal-semiconductor interface, which creates a potential barrier and depletion layer in the semiconductor interface [26]. The current flow pass this barrier shown in Figure 1.3.1 can be achieved by (1) thermionic emission, (2) electron tunneling, (3) electron – hole recombination, (4) electron diffusion, and (5) hole diffusion at the metal-semiconductor interface [26].

Photoconductor detectors involve metal-semiconductor-metal (MSM) structure with metal ohmic contacts and the semiconductor acting as a light sensitive resistor [13, 28]. The ohmic contacts are junctions with a resistance or potential barrier at the metal-semiconductor interface that is negligible compared to the resistance of the total semiconductor device [26]. The low potential barrier results in current flow being dominated by thermionic emission and charge tunneling [26]. Thermionic emission is when charges with energy greater than the energy barrier, ϕ_{Bn}, flow to the metal, and charge tunneling is a quantum mechanical process by which the electron wave function tunnels through the energy barrier [26]. In an ohmic contact MSM photodetector, the electrons can cycle through the photoconductor system many times do to low resistance which can result in high photoresponsivity. ZnO photoconductors MSM structure have been fabricated

through molecular chemical vapor deposition (MOCVD) and have shown a responsivity of up to 400 A/W at 5.0 V bias [29], and 124 A/W at 5.0 V for RF magnetron sputtered films [30].

On the contrary, MSM photoconductors can have Schottky contacts instead of the ohmic contacts, where the Schottky contact has a much larger energy barrier at the metal-semiconductor interface. Thermionic emission is the dominant means of electron transport from semiconductor to metal for the Schottky contact do to the large barrier minimizing tunneling, diffusion, and recombination at the interface [26]. The large barrier allows for low noise and high speed do to mainly high energy electrons contributing to the photocurrent. As a result, these devices sacrifice the benefit of low energy electrons contributing to the photocurrent, which results in lower responsivity [26, 31, 32]. Schottky based MSM photodetectors fabricated through ZnO epitaxy films on Ag exhibited a small photoresponsivity of 1.5 A/W at a 5.0 bias [33], and 11.3 μA/W for laser assisted beam molecular deposition grown ZnO films [31].

1.4 *Bulk and Nanostructured ZnO UV Devices*

In bulk semiconductors the electronic behavior can be theoretically described by taking an infinite lattice approximation, as a result the charges lack confinement, and the surface effects become negligible [34]. In addition, a perfect bulk semiconductor can gain one electron in the conduction band for one photon, and so the maximum obtainable quantum efficiency is 100% [34]. Unlike the bulk, ZnO nanostructures can feel the effects from the surface when the size approaches scales on the order of the Debye length (~20 nm) [4-6] and the exciton Bohr radius (~ 1 nm) [2, 3] of a semiconductor. In particular, the Debye length λ, which describes depth penetration of electromagnetic fields in the semiconducting material, is the scale the local conductivity of the semiconductor can be drastically changed by dopants on the surface [6]. For ZnO the surface has

many oxygen vacancies that cause oxygen gas to be loosely attached to the surface of zinc oxide through capturing free electrons (Figure 1.4.1 a), this process can be described by [13, 22, 28]:

$$O_2(g) + e^- \rightarrow O_2^-(ad)$$

The captured electrons create a depletion region in ZnO with a thickness of λ, which can lower the dark current in both bulk and nanostructure ZnO, however the effect is more dramatic in nanostructure ZnO (Figure 1.4.1). Under UV illumination the nanostructure ZnO also can quickly recover the captured electron by recombining with holes that migrate to the surface (Figure 1.4.1 c). This oxygen desorption process can be described by [13]:

$$h^+ + O_2^-(ad) \rightarrow O_2(g)$$

The hole and absorbed oxygen recombination leads to the ZnO obtaining an electron from the oxygen, resulting in two electrons for one photon for a maximum quantum efficiency of 200%; in addition, combined with low dark current this can lead to large photoconductive gain and large on-off ratio [13].

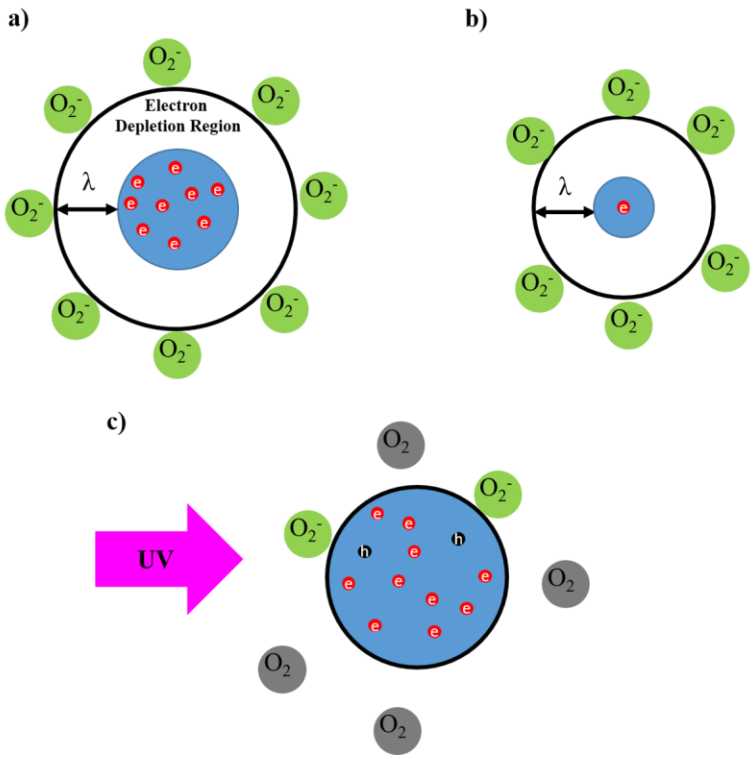

Figure 1.4.1 (a) depicts a larger piece of ZnO than (b), the Debye length λ is the depth of the electron depletion caused by absorbed oxygen.

In Table 1 is a comparison of the performance results of both the bulk and nanostructured ultraviolet photodetectors. Given the power, the photocurrent for both bulk films are on the order of microamps, whereas, the thin films have photocurrent on the order of milliamps. In fact, both thin films have photoresponsivity on the order of the bulk film, which is fabricated through high quality method of MOCVD. However, the thin films have larger rise and fall times do to slow oxygen absorption-desorption process on the surface.

Fabrication	*Morphology*	*Rise Time*	*Fall Time*	*Power*	*Photoresponsivity*	*Ref.*
MOCVD	Bulk Film (1 µm)	1 µs	1.5 µs	6.4 nW	400 A/W	[29]

Hydrothermal	Bulk Film (0.5 mm)	--	--	~1.4 mW	~0.26 A/W	[35]
RF Sputtering	Thin Film (211 nm)	0.82 ms	0.64 ms	37.5 µW	124 A/W	[30]
Spray Pyrolysis	Thin Film (~396 nm)	16 s	18 s	0.9 µW	788 A/W	[36]

Table 1 Summary of bulk and thin film photoconductor UV photodetectors fabricated by different methods.

1.5 *ZnO/Graphene Nanohybrids*

ZnO nanostructures/graphene nanohybrids are of increasing interest do to graphene's unique properties such as high carrier mobility, optical transmittance of ~97.7% to white light, zero bandgap, chemical stability, and flexibility [37-39]. The band structure of graphene has benefits and negatives, and one of the primary benefit is the high charge mobility. The large charge mobility allows for very small transit time, $\tau_{transit}$. A small transit time in combination with a large charge life time (τ_{life}) can result in very large photoconductive gain. In addition, graphene is a 2D material so the whole material acts as a surface, which allows graphene to be easily doped to be hole dominant (Figure 1.5.1 a) or electron dominant (Figure 1.5.1) by adjusting the fermi level by applying a gate voltage [37, 40].

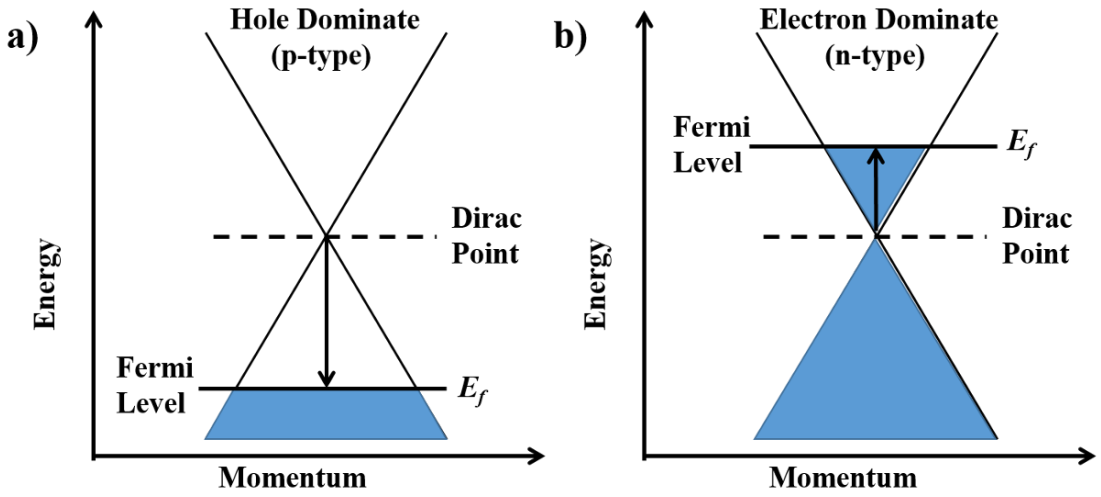

Figure 1.5.1 The hole dominant and electron dominant graphene fermi levels are depicted in (a) and (b) respectively.

Nanostructure ZnO/graphene hybrids operate by energy band misalignment of the conduction band of ZnO relative to graphene. ZnO has a higher conduction band energy compared to graphene as is depicted in Figure 1.5.2 [41, 42]. The electrons desire a lower energy state so the excited electrons in ZnO under UV light will transfer to graphene leaving behind a hole in ZnO. This hole applies a positive gate to graphene, which results in a doping of a perfect graphene lattice, this doping will shift the fermi level above the Dirac point of a perfect graphene lattice, if the gate was negative then the fermi level would be shifted below the Dirac point and the graphene will have p-type doping [37, 40-42].

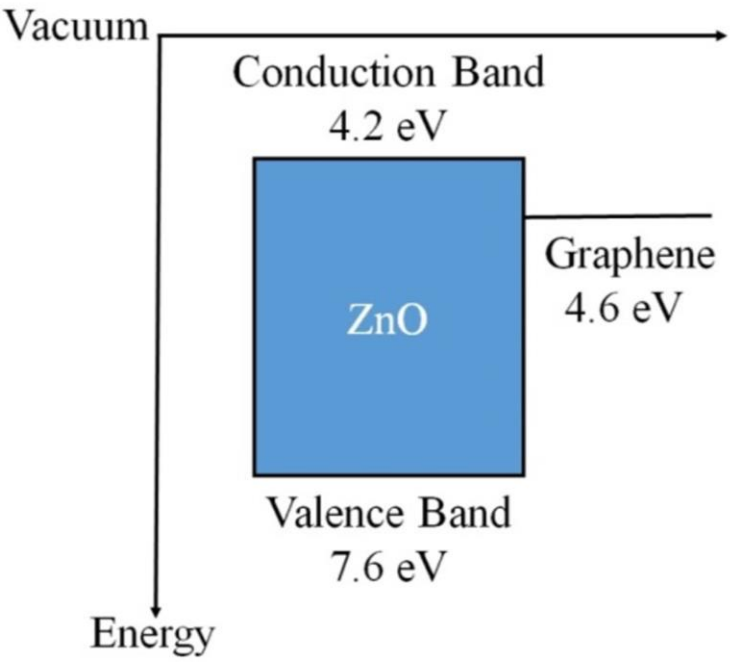

Figure 1.5.2 The conduction and valence band of ZnO compared to graphene energy level.

Nanostructures of ZnO in combination with graphene's high carrier mobility can facilitate charge carrier transport more efficiently than conventional materials, yielding an extraordinary photoresponsivity (R) in exceeding 10^4 [42-45]. In addition, the uniform transmittance of ~ 97.7% per graphene sheet to white light makes ZnO/graphene hybrid perfect for visible-blind optoelectronics with a photoconductive gain as high as 10^6 [45], and 10^7 for ZnO quantum dot/graphene hybrids has been demonstrated [42].

Chapter 2

Material Processing and Characterization

2.1 *Material Synthesis*

All zinc oxide (ZnO) materials used in this thesis were fabricated via a hydrothermal method, the materials synthesized involve ZnO nanowires (NWs), ZnO quantum dots (QDs), and ZnO porous thin films. The graphene used in these experiments are grown through chemical vapor deposition (CVD) on copper foils then transferred through a transfer process that will be described in the next section. The benefits of hydrothermal methods and CVD methods is that they can be scaled up for mass production. Furthermore, hydrothermal methods in particular can be used as an ink in direct printing applications, which can reduce waste and cost.

2.1.1 Graphene Transfer Process and Cleaning

Graphene was grown on Cu foil via the CVD method. To transfer graphene, the graphene/Cu foil was spin-coated with Poly(methyl methacrylate) (PMMA) and baked for 1.0 hour in an 80 ^{o}C oven. The copper was then etched away with iron chloride leaving behind a graphene/PMMA film that was floated in deionized (DI) water several times for cleaning, after which the graphene/PMMA film is transferred to a SiO_2/Si substrate. The substrate/graphene/PMMA sample was baked for 1.0 hour at 80 ^{o}C, then acetone and isopropanol is used to wash away the PMMA. Then the sample is finished with annealing in a furnace at 400 ^{o}C for 15 minutes under argon and hydrogen gas flow at 500 sccm to rid of any residual PMMA and surface contaminates. To grow ZnO on the surface of graphene, the graphene surface was

cleaned with acids (0.1 M HCl) and bases (0.1 M NaOH) for 1.0 hour each, this time is adjusted if the substrate is sensitive to acid and base etching, after which graphene is cleaned with DI water several times.

2.1.2 ZnO Nanowire Hydrothermal Growth

Zinc oxide nanowires were synthesized by mixing zinc nitrate $Zn(NO_3)_2$ into deionized water. This mixture allows for Zn^{2+} and NO_3^- ions to form in the mixture, then ammonia hydroxide is added to form NH_4^+ and OH^- ions, and NH_3 [46]. The amount of ammonia added is determined by the pH target, for nanowires to form a pH in the range of 10-11 is ideal [46]. The reactions occur at a temperature of 80-90 ^oC, which can be described by the following chemical reaction equations [46]:

$$NH_3 \cdot H_2O \leftrightarrow NH_4{}^+ + OH^-$$

$$NH_3 \cdot H_2O \leftrightarrow NH_3 + H_2O$$

$$Zn^{2+} + 4NH_3 \leftrightarrow Zn(NH_3)_4{}^{2+} + 4OH^- \leftrightarrow Zn(OH)_4{}^{2-} + 4NH_3$$

$$Zn(OH)_4{}^{2-} \leftrightarrow ZnO + H_2O + 2OH^-$$

This reaction process allows the ions to attach to surfaces through Coulomb and Van der Waals attraction. However, self-nucleation lacks precise control over the density of nanowires on the surfaces. Often a seed layer is used to control the nucleation density of the nanowires. For the seed layer solution, a mixture of zinc acetate, DI water and methanol ultrasonicated for 30 minutes is used.

2.1.3 Zinc Oxide Quantum Dot Synthesis

Zinc oxide quantum dots were synthesized by mixing 1.0 mmol of zinc acetate dihydrate, 10 ml of ethanol and stirred for 70 ^{o}C for 1.0 hour [41]. The mixture was then cool to room temperature, then in a separate container, a mixture of potassium hydroxide (1.7 mmol) added to 10 ml of ethanol, and sonicated for 1.0 hour [41]. Both solutions are then cooled down to 0 ^{o}C via ice bath, afterward drop by drop the potassium hydroxide mixture was added to the zinc acetate dehydrate mixture and allowed to sit in a refrigerator (4 ^{o}C) for 24 hours [41]. Hexane (30 ml) was added and centrifuged at 4000 RPM, from which ZnO QDs are extracted and cleaned three times with an ethanol and hexane mixture of same ratio, then allowed to air dry for 10 hours afterwards placed in ethanol for storage [41]. The main reaction equations that lead to ZnO QDs, the chemical process are given by the following [41]:

$$Zn^{2+} + 2OH^{-} \leftrightarrow Zn(OH)_2$$

$$Zn(OH)_2 + 2OH^{-} \leftrightarrow [Zn(OH)_4]^{2-} \leftrightarrow {ZnO_2}^{2-} + 2H_2O$$

$${ZnO_2}^{2-} + H_2O \leftrightarrow ZnO + 2OH^{-}$$

$$ZnO + OH^{-} \leftrightarrow ZnOOH^{-}$$

The last reaction results in a layer on the ZnO QDs surface that can degrade charge transfer from ZnO QDs, this can be fixed with careful control of the hydrolysis process, and aging in a solution of ethanol [41].

2.1.4 Inks for Printing ZnO

The ink used for printing ZnO is a ZnO precursor (ZnOPr) that is a mixture of 0.3 M zinc acetate dihydrate, 0.3 M ethanolamine dissolved in 2-methoxyethanol and sonicated until completely dissolved usually 10 min. or longer [47]. This ink was mixed with ZnO quantum dots to make the ZnO/ZnO QD composite ink (ZnOPrQDs). When the ZnO precursor ink is heated on its own to 350 ^{o}C in air at atmosphere, it will decay into zinc oxide by the following chemical reactions [48]:

$$Zn(CH_3COO)_2 + 2H_2O \xrightarrow{heat} Zn(CH_3COO)_2 + 2H_2O \uparrow$$

$$4Zn(CH_3COO)_2 + 2H_2O \xrightarrow{heat} Zn_4O(CH_3COO)_6 + 2CH_2COOH \uparrow$$

$$Zn_4O(CH_3COO)_6 + 3H_2O \xrightarrow{heat} 4ZnO + 6CH_3COOH \uparrow$$

$$Zn_4O(CH_3COO)_6 \xrightarrow{heat} 4ZnO + 3CH_3COCH_3 \uparrow + 2CO_2 \uparrow$$

2.2 *Device Fabrication*

2.2.1 Electrodes

The Au electrodes were deposited on silicon dioxide (SiO_2)/Silicon (Si) wafer with an electron beam evaporator. The gold electrodes for testing stability and ZnO nanowires have a channel length of 0.3 mm and a width of 3 mm. The electrodes for printing ZnO films used interdigitated electrodes with a 100 μm channel width and 1800 μm teeth length. The SiO_2 is 500 nm thick for all the substrates used and the Si layer underneath is heavily p-doped.

2.2.2 ZnO Nanowire/Graphene Nanohybrid UV Photodetector Fabrication

The solution was spin coated on the sample surface then annealed at 200 C^0 for 3 minutes, this can be done for as many times necessary, after the final spin coat the sample was annealed at 250 C^0 for 30 minutes to evaporate water and methanol. The seed layer provides a reactive surface for zinc nitrate and ammonia hydroxide hydrothermal growth solution, since graphene is a relatively non-reactive surface. A seeded and seedless method were fabricated to compare device performance (Figure 2.2.1).

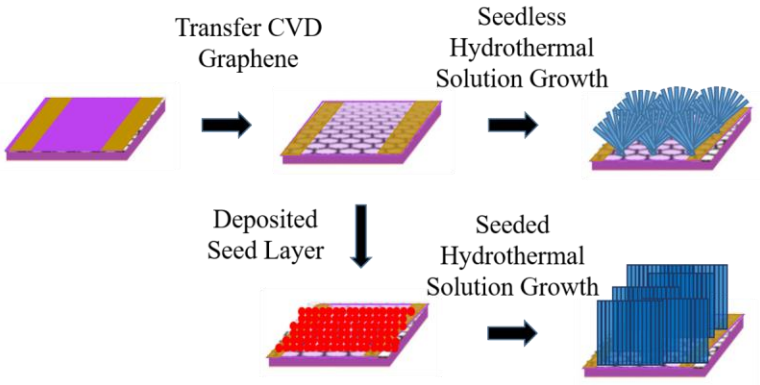

Figure 2.2.1 CVD graphene was transferred onto Si/SiO_2 wafers with deposited gold electrodes. Samples are then placed in their perspective growth solution then placed in an oven at 80 ^oC.

The seed layer solution was made of 0.818 g of zinc acetate, 0.25 ml of DI water and 42 ml of methanol, which was ultrasonicated for 30 minutes. The solution was spin coated on the sample surface at 3500 RPM for 1.0 minute and then annealed at 200 °C for 3 minutes, this was done five times, and after the final spin coat the sample was annealed at 250 ^oC for 30 minutes. The seedless sample is then floated in 100 ml of an aqueous 10 mMol zinc nitrate hexahydrate solution, ammonia hydroxide is added until the total pH is approximately 10-11. The seeded sample is floated in the same volume of solution and same pH level with a different concentration of zinc nitrate (2.0 mMol). The floating substrate samples and solution are placed in the oven at

80 ^{o}C. The seedless substrate requires extra steps of renewing the solution ever two hours for 4-9 hrs. depending on the sample. This is to ensure dense nucleation. The seed layer samples required no renewing of solution and is finished after 3 hrs. since the seed layer is enough for dense nucleation

2.2.3 Printing Porous ZnO Film UV Photodetector

To simplify the conventional method of spin coating and annealing, printing is becoming an attractive alternative. Inkjet printing unlike spin coating does not require large deposits of material onto the surface. Instead inkjet printing can target a specific area for depositing materials, which avoids ink waste and etching. The inkjet printer operates by depositing ink via ultra-sonication of a glass capillary. The arm has mobility in all directions allowing for printing on multiple surfaces at different heights. Figure 2.2.2 illustrates schematically the two ZnO nanostructure photoconductive photodetectors printed using ZnOPr (Figure 2.2.2 a) and ZnOPrQDs (Figure 2.2.2 b) inks, respectively.

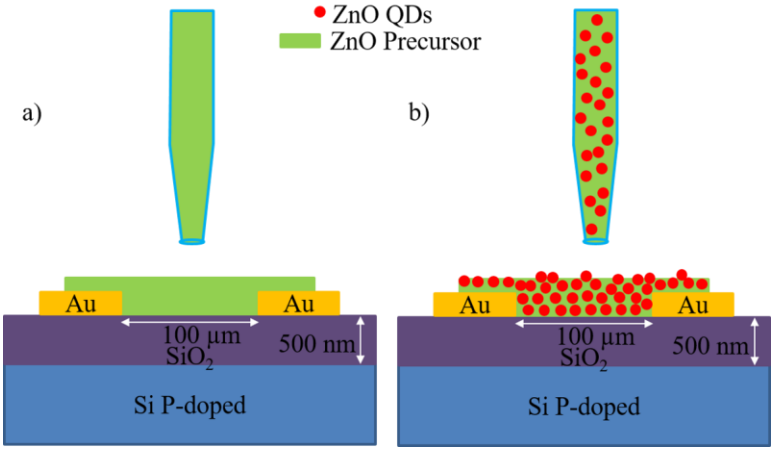

Figure 2.2.2 (a) Printer tip that deposits ZnO precursor through ultrasonication on electrodes Au electrodes, (b) shows a similar process only with ZnO quantum dots mixed with the precursor.

2.3 *Characterization*

2.3.1 Graphene Characterization

Scanning electron microscopy and Raman spectra were taken of graphene/SiO_2/Si wafers to check for crystallinity of graphene. The graphene has two distinctive peaks, a symmetric large peak called the 2D peak at ~2700 and a smaller G peak at ~1580 (Figure 2.3.1) [49]. The 2D peak is very symmetric and the G peak less than half the size of the 2D peak indicating highly crystalline graphene [49].

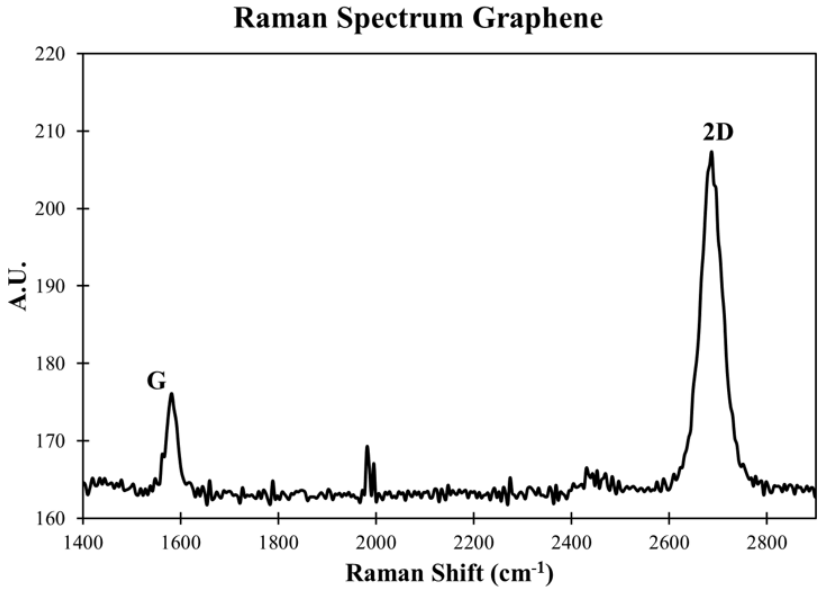

Figure 2.3.1 Raman spectrum of graphene indicated by the symmetric 2D peak and the small G peak relative to the 2D.

2.3.2 Zinc Oxide Nanowire Characterization

Zinc oxide nanowires show a large affect from the density of seeds available for the nanowires growth. The Raman spectrum for graphene with and without a seed layer is in shown in Figure 2.3.2 a. The Raman shows a clear symmetric 2D peak and a smaller G peak at around

~2700 cm^{-1} and ~1580 cm^{-1}, with a negligible D band (~ 1350 cm^{-1}) indicating transferred monolayer graphene. After adding the seed layer there is a shift in the peaks indicating a heavy doping from the seed layer [50-52]. In Figure 2.3.2 a, the graphene shows the normal transmittance and experiences some band bending in the UV range. After introducing the zinc oxide seed layer there is absorption starting at 600 nm (Figure 2.3.2 b), indicating defect states in the ZnO seed layer and at the interface between ZnO and graphene, afterward ZnO follows the usual UV absorption edge at around ~380 nm.

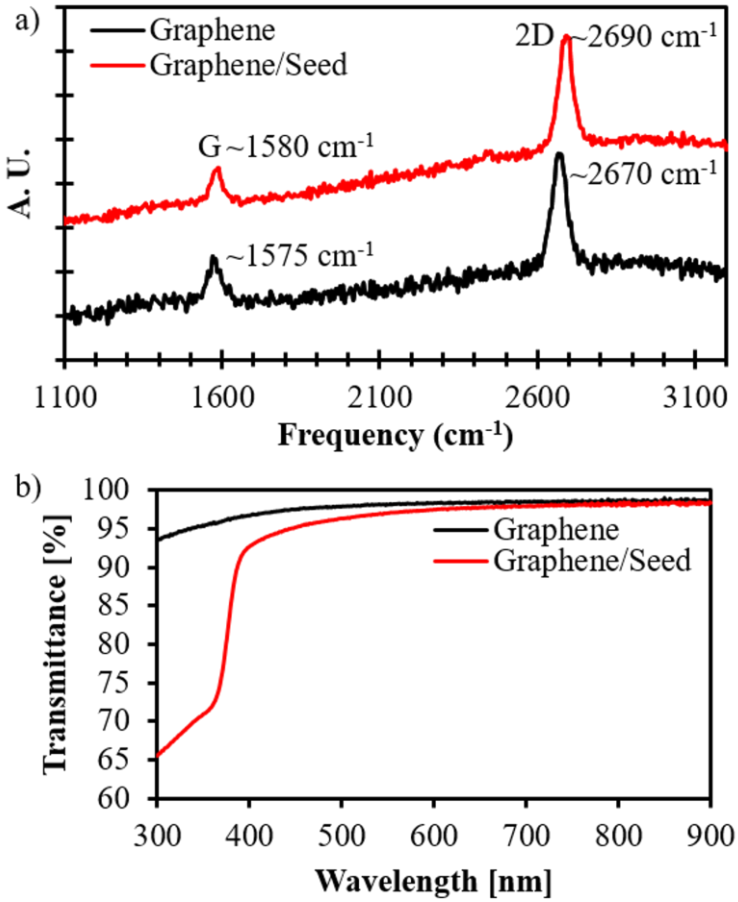

Figure 2.3.2 (a) Raman spectrum of graphene with (red) and without (black) the seed layer and (b) the transmittance of graphene with (red) and without seed (black).

SEM images of the different surfaces one being seedless and the other seeded are shown in Figure 2.3.3a and Figure 2.3.3 b respectively. The seedless surface has less nucleation sites do to graphene's inert properties, however, imperfections in CVD graphene morphology allow for dangling bonds to serve as nucleation sites. Lower nucleation sites result in larger nanowire and growth in all directions (Figure 2.3.3 c), whereas, denser seeding forces nanowires to grow perpendicular to the seeded surface (Figure 2.3.3 d). The horizontal growth is motivated by the adjacent nucleation sites sapping reactions, causing nanowires to grow perpendicular to the surface where more reactants in solution are available (Figure 2.3.3 d). The seedless grown nanowires are depicted in Figure 2.3.3 e have a diameter of ~1 µm, and ~200 nm for the seedless grown nanowires (Figure 2.3.3f).

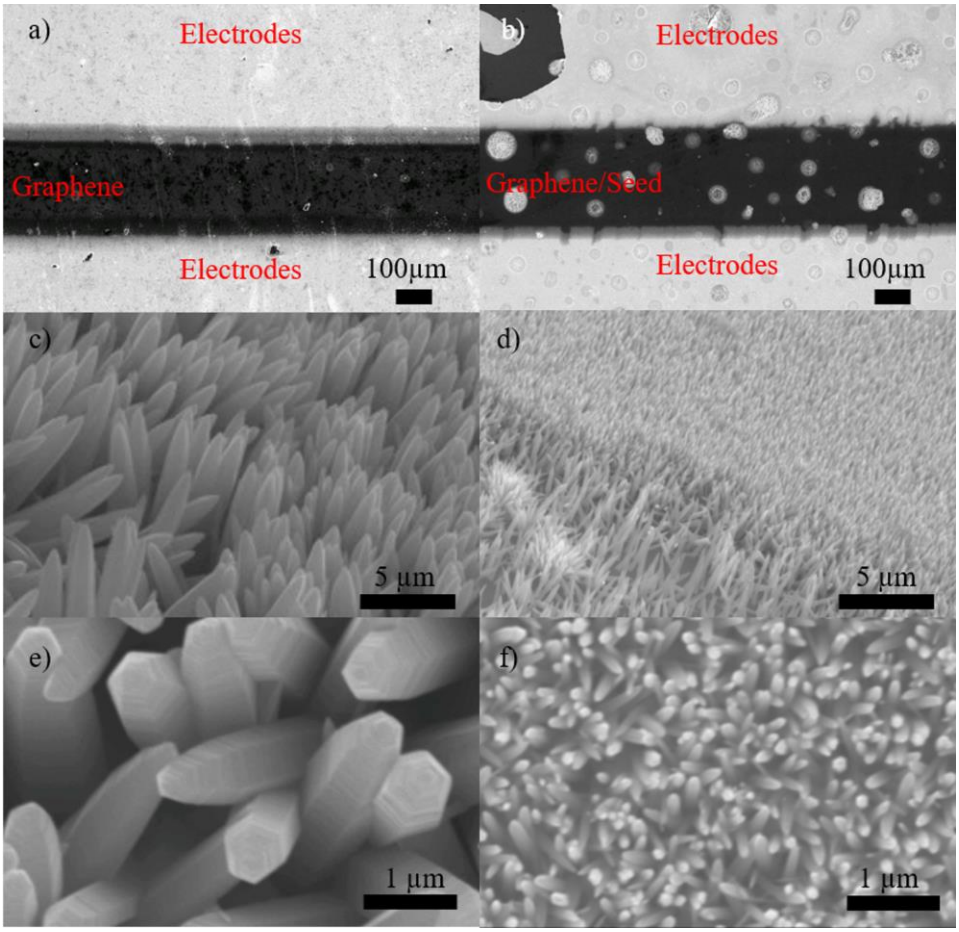

Figure 2.3.3 (a) and (b) show the seedless and seeded samples respectively before nanowire growth of graphene/SiO_2/Si wafer. (c) After hydrothermal growth of ZnO the seedless samples show nanowire diameter on the order of 1.0 μm, and an alignment more dispersed than seeded graphene shown in (d). Seeded samples in (d) have a nanowire diameter from ~200 nm, depending on the density of seeds. (e) and (f) show a top view at large magnification.

Figure 2.3.4 compares the transmission electron microscopy (TEM) and high resolution TEM (HRTEM) images of the ZnO NWs fabricated using the seedless and seeded graphene processes. The former exhibits high-quality crystalline structure with the NW axial orientation along the [0001] of ZnO, with tip diameters on the order of 100-500 nm and stem diameters ranging from 1.0-3.0 μm as shown in Figure 2.3.4 a [46]. The seeded grown ZnO-NWs have similar crystalline structure (Figure 2.3.4 b); however, the NW tip and stem diameter of the ZnO-NWs range between 10-50 nm and 70-300 nm, respectively [46]. Furthermore, non-uniformity in the NW crystallinity can be seen in Figure 2.3.4 b, and is more obvious with HRTEM of the bottom (Figure 2.3.4 c) and tip (Figure 2.3.4 d), showing poor crystallinity especially at the bottom of the ZnO-NW. In contrast, a more uniform crystallinity on the seedless-grown ZnO-NWs (Figure 2.3.4a) is observed [46]. This suggests the crystallinity of the ZnO seed layer may not be uniform, which affects the uniformity, crystallinity, and the optoelectronic properties of the ZnO nanohybrid devices.

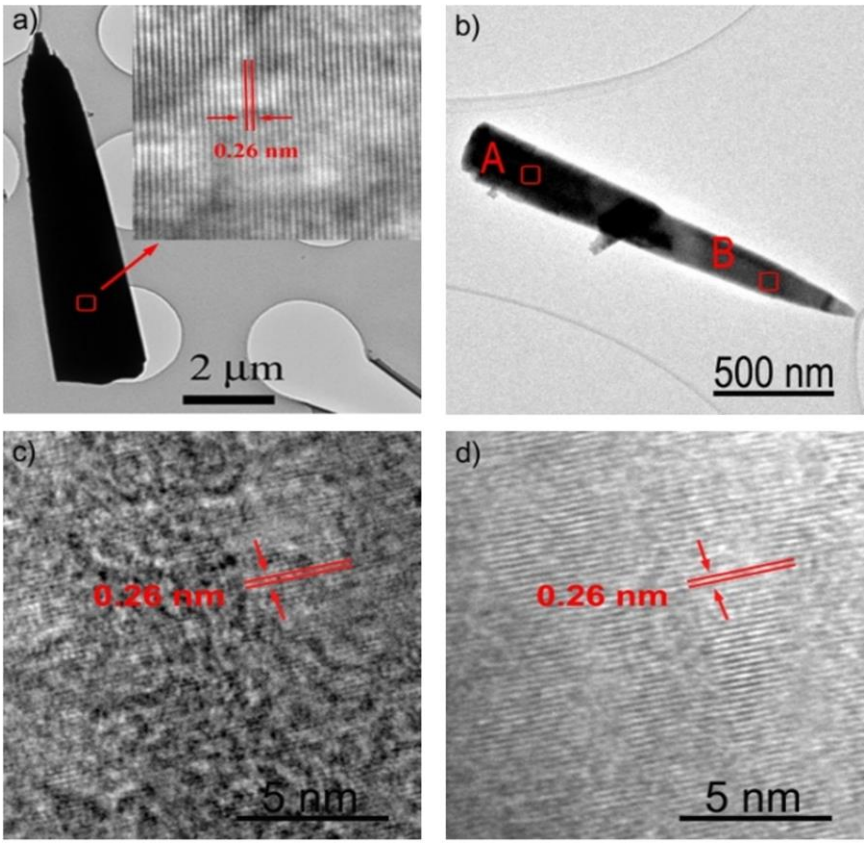

Figure 2.3.4 (a) Typical TEM image of a seedless grown ZnO NW and inset is enlarged framed area of the bottom of ZnO NW [46]. (b) Typical TEM images of a seed-grown ZnO NW, (c-d) HRTEM image of the framed areas of the same ZnO NW on its (c) tip and (d) bottom, revealing the ZnO [0001] fringes perpendicular to the wire axis on average separated by 0.26 nm, indicating the high crystalline ZnO growth along the ZnO [0001] direction.

2.3.3 Zinc Oxide Inks and Printed Film Characterization

Thin films of spin coated ZnO precursor show a mesoporous morphology. The nanoporous morphology is ideal for detector application since there is an increased surface area and decreased dark current do to grain boundaries. ZnO nanoparticles that make up the nanoporous film fall in the Debye length of zinc oxide at a diameter range of 20 – 40 nm (Figure 2.3.5) [47].

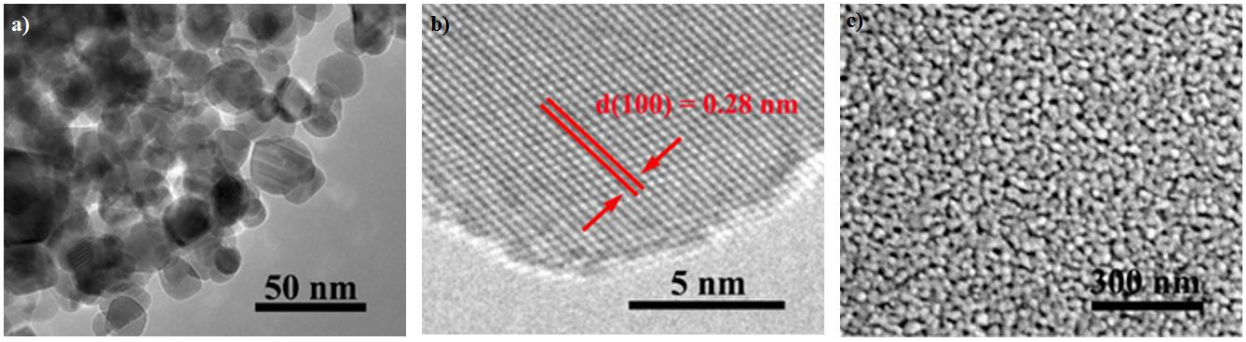

Figure 2.3.5 (a) shows the nanoparticles that make up the thin film and how they have merged into a film [47]. (b) shows an individual particle and the lattice spacing, all together the particles make a film shown in (c) [47].

Printing the same precursor via ultrasonic inkjet printing produces very different results with the uniformity subject to variations in the surface and ink. The ZnO QDs used in this work show a spherical shape with the diameter distribution ranging from 1.5 nm – 6 nm (Figure 2.3.6), the morphology of the two samples printed with ZnOPr and ZnOPrQDs differs considerably as shown in the SEM images (Figure 2.3.7). Without ZnO QDs in the $Zn(AC)_2$ precursor ink, the samples have a highly rough and porous morphology (Figure 2.3.7 a-b). The pores have irregular shapes with dimensions in the range of sub-to-few micrometers. It is understandable that the formation of the pores may closely relate to the surface of the substrate. The hydrophobic surface of the SiO_2/Si substrates used in this work plays a critical role in forming the porous microstructure of the ZnO nanostructure films printed from the ZnOPr ink due to the large contact angle of the ink on the substrate surface. In contrast, the addition of the ZnO QDs into the $Zn(AC)_2$ precursor ink, the printed ZnO-nanostructure films look primarily dense and smooth except some ridges and valleys (Figure 2.3.7 c-d). No large-dimension pores are visible, which indicates the presence of the ZnO QDs alters the contact angle of the ZnOPrQDs ink with the substrates to promote the even spread of the ink on the substrate surface.

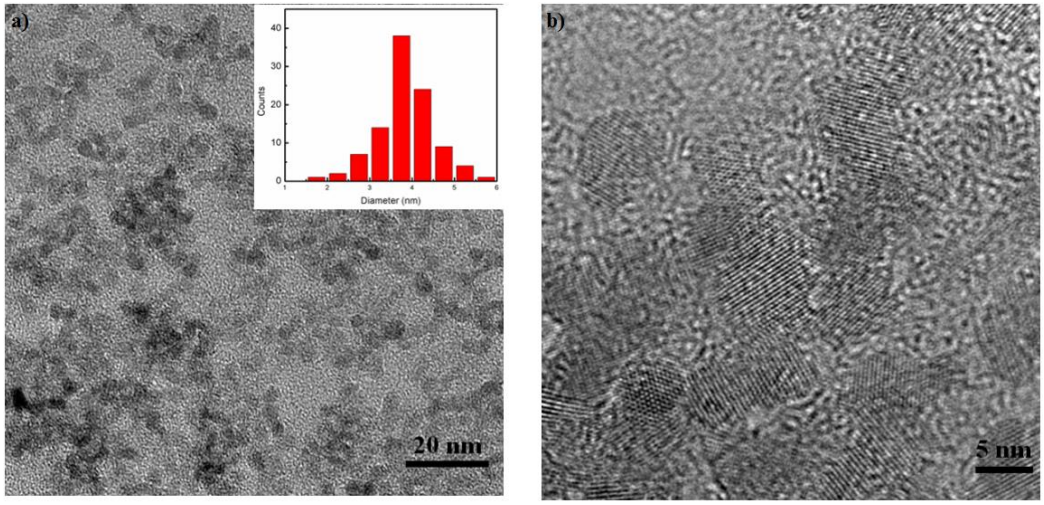

Figure 2.3.6 The ZnO QDs show a majority size range below 10 nm from inset in (a). (b) ZnO QDs look to be around 3-6 nm.

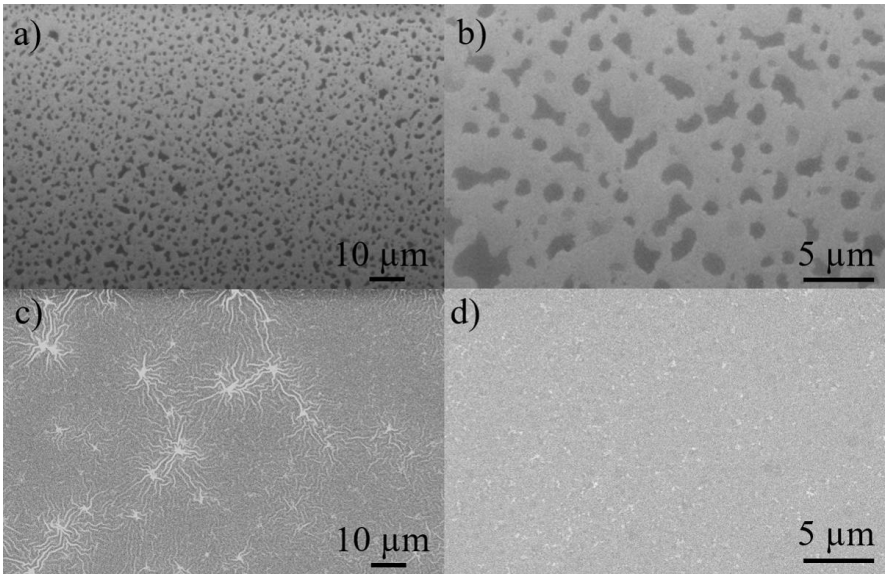

Figure 2.3.7 (a) and (b) show a single layer of printed ZnOPr at different magnifications 10 µm and 5 µm respectively. In (c) and (d) is a single layer of printed ZnOPrQDs of similar scales to (a) and (b), respectively.

Under transmission electron microscopy (TEM) the printed ZnOPr (Figure 2.3.8 a) and ZnOPrQD (Figure 2.3.8 b) ink shows ZnOPr films have less grain boundaries than ZnOPrQD films, and under high resolution transmission electron microscopy (HRTEM) grain boundaries are absent from ZnOPr (Figure 2.3.8 b) and present in ZnOPrQDs do to quantum dots (Figure 2.3.8 d). Furthermore, ZnO nanocrystallites are visible in both cases, but the dimension of the crystallites in the ZnOPr sample is larger than that of the ZnOPrQDs sample in Figure 2.3.8 a and c, respectively.

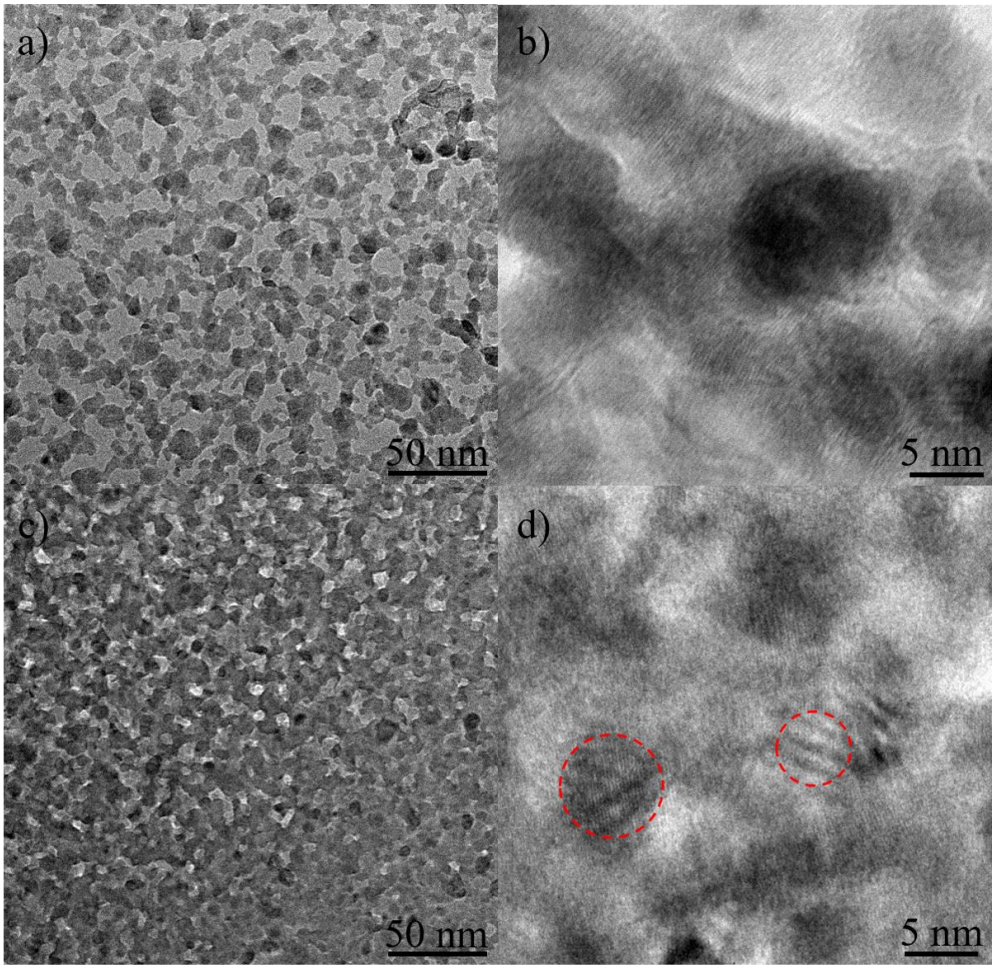

Figure 2.3.8 (a, c) TEM and (b, d) HRTEM images of a single layer of printed (a, b) ZnOPr and (c, d) ZnOPrQDs films.

Chapter 3

ZnO Nanowire/Graphene Nanohybrid Ultraviolet Photoconductor

3.1 *ZnO Nanowire/Graphene Nanohybrids*

A critical step towards a high-performance ZnO/graphene nanohybrid devices is in controlling the dimension of the ZnO nanostructure down to the Debye length for optimal electron depletion effect and the ZnO/graphene interface for efficient charge transfer. Methods for depositing ZnO nanostructures on graphene include sputtering, molecular chemical vapor deposition (MOCVD), hydrothermal, and spin-coating. Unlike MOCVD and sputtering techniques which can be costly, time consuming, and damaging to graphene, the solution processes such as hydrothermal and spin-coating have the merits of low cost, low processing temperature and no vacuum [23, 28, 53]. ZnO NWs have been studied heavily for sensor applications, such as gas sensing [54, 55] and UV detection [44, 45, 56] do to the large surface area of the ZnO NWs, and in particular, vertically aligned ZnO NWs on graphene are of interest [19, 46, 57]. Using a solution process allows for control over the NW morphology, length, and diameter via solution parameters such as temperature, reactants, and pH using either a seeded method [24, 57, 58] or seedless method on graphene [19, 46, 58]. Seedless fabrication requires longer growth time and careful tuning of pH to achieve dense ZnO NWs of diameter in the range of microns [56]; in contrast, the seeded devices have less growth time and diameters on the order of nanometers [59, 60].

When dealing with nanomaterials, interface is a major contributor to device performance, so the effect of a seed layer on graphene is of great concern. In this section, a ZnO seed was employed on the graphene surface to evaluate the effect on the ZnO NW morphology and ZnO

NW/graphene interface on UV device performance. Graphene being an ambipolar material can have the fermi level changed by applying an electric field on graphene. The fermi level is the highest occupied energy level for electrons, and is either shifted above or below the Dirac point of graphene, the Dirac point being where the conduction and valence energy bands meet [40]. Since zinc oxide is n-type, the ZnO will apply an intrinsic negative gate pushing graphene to have hole dominance, p-type. Once ZnO is illuminated with UV, excitons are generated and the holes recombine with electrons trapped by absorbed oxygen. The electrons then transfer to graphene do to energy band offset, leaving the holes behind which apply a positive gate giving graphene n-type behavior. These charge dynamics play a major role in the optoelectronic properties of the ZnO-NW/graphene nanohybrid photodetector.

3.2 *Photovoltaic Properties of ZnO Nanowire/Graphene Photodetector*

The morphology between the two devices is significantly different as described in Section 2.1.2 where the seeded device (Figure 2.3.3 b, d, f) gives rise to a denser nucleation and smaller wires (Figure 2.3.4 b); whereas, a seedless graphene surface (Figure 2.3.3 a, c, e) gave rise to less nucleation, and thicker wires (Figure 2.3.4 a). However, the seed layer contributed to band defects as seen in the absorption spectrum in the 500 nm range (Figure 2.3.2 b), and low crystallinity at the graphene nanowire base (Figure 2.3.4 c) despite decent crystallinity at the top of the nanowire (Figure 2.3.4 d). These morphological property difference and surface interaction cause a dramatic change in the photovoltaic performance of the ZnO NW/graphene nanohybrid photoconductor. The current-voltage characteristic curves are depicted in Figure 3.2.1 a and b, for the seedless and seeded samples respectively. The photoresponsivity at 5.0 V and a wavelength of 340 nm is 4.12

A/W and 728 A/W for the seedless and seeded cases respectively, which is two orders of magnitude increase.

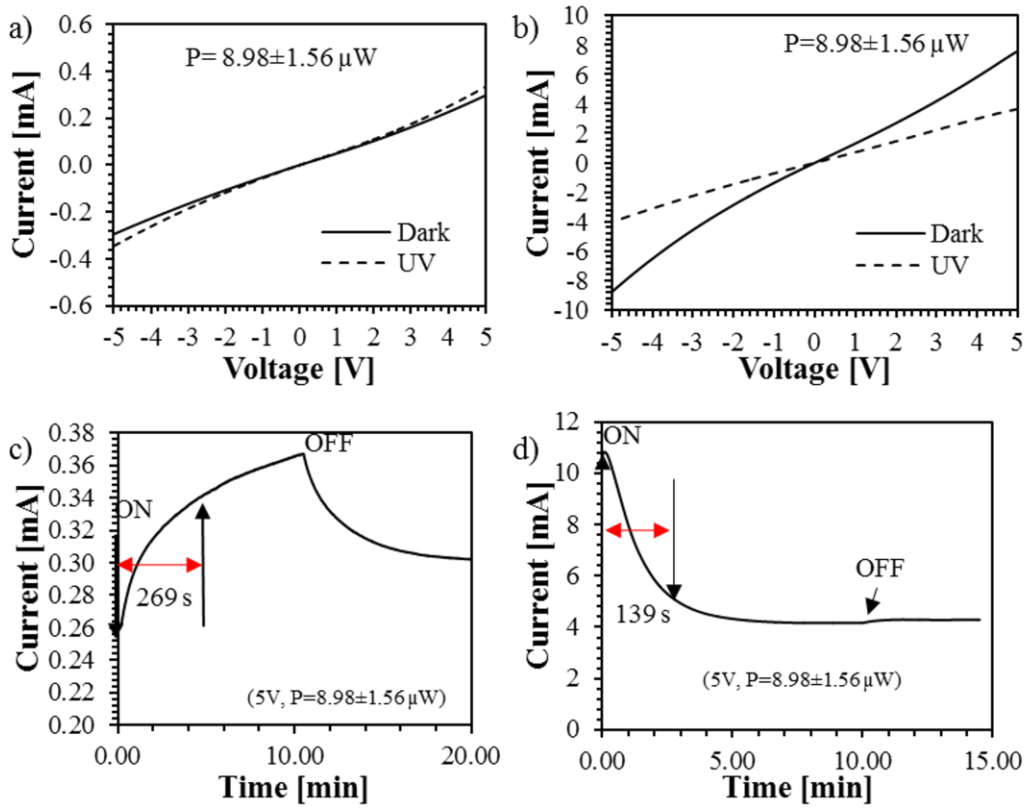

Figure 3.2.1 Photovoltaics of samples in response to 340 nm at 8.98 ± 1.56 μW. The I-V characteristics curves for (a) the seedless ZnO-NW/graphene nanohybrid and (b) the seeded sample, and the dynamic response of the seedless (c) and the seeded (d) samples.

The seedless and seeded graphene surface for nanowire growth also have differing dynamic behavior under UV illumination as depicted in Figure 3.2.1 (c, d), which shows a slow rise time for the seedless (269 s) and seeded (139 s) samples respectively. However, do to the slow the process of oxygen adsorption/desorption on the zinc oxide surface, the rise times are long. The fall times are extremely slow for both seeded and seedless samples and depict no noticeable return to the initial value until after an hour or more. The seedless sample shows some initial decay whereas

the seeded sample does not, this is likely do to many charge trap states at the interface do to the seed layer. Furthermore, the seeded sample shows a negative photocurrent, this is do to n-type ZnO which provides a positive doping on graphene and a shift of the fermi level below the Dirac point (Figure 3.2.2a) [41]. When a ZnO seed is introduced it can provide heavy p-type doping in graphene (Figure 3.2.2b). When ZnO is illuminated with UV light the electrons are transferred to graphene and holes become trapped at the ZnO/graphene interface. The trapped holes provide n-doping to graphene and push the fermi level back to the Dirac point Figure 3.2.2 (a, b). In the case of the seedless sample there is less ZnO seed at the interface to cause massive p-doping, but for the seeded sample the p-doping could be very large and cause a bigger shift of the fermi-level below the Dirac point. The larger the p-doping from ZnO seed layer could result in negative photocurrent (Figure 3.2.2b).

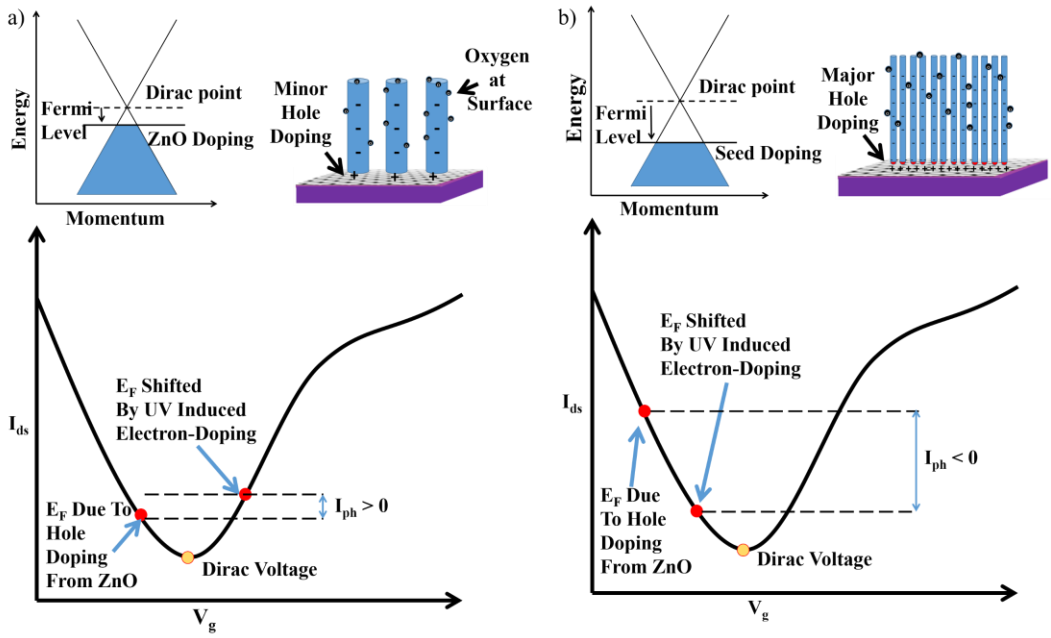

Figure 3.2.2 (a) The doping from the ZnO on the surface of seedless graphene and for (b) the seeded graphene.

Chapter 4

Inkjet Printing ZnO Nanostructure Photodectors

4.1 *Inkjet Printing*

Ultrasonic inkjet printing offers a cost effective method for integrating devices based on nanomaterials with CMOS by avoiding surface contact, allowing direct deposition, low-waste and mass scalability [61, 62]. To control the ink dispersion in terms of ink-drop morphology, thickness, and diameter, the prepared ink must have the right Reynolds, Weber, and Ohnesorge numbers, which are dependent on the ink density, travel velocity, viscosity, and surface tension [63, 64]. Among these three numbers, the Ohnesorge number N_O is the most important. N_O is the ratio of the Weber number N_W and Reynolds number, N_R, and is given by: $N_O = \frac{\sqrt{N_W}}{N_R} = \frac{\eta}{\sqrt{\gamma\rho\alpha}}$, where η, γ, ρ, and α are the ink viscosity, surface tension, density, and characteristic length respectively [63, 64]. The Z parameter, which is the inverse of the Ohnesorge number, indicates ink droplet formation. For high viscosity or high fluidity, a Z parameter of $Z<1$ or $Z > 10$ respectively is preferred, for printing the range $1<Z<10$ is ideal [63, 64].

4.2 *Printing Inks for ZnO films*

In printing, the selection of the inks depends on the specific material, printing surface, and application. Inkjet printed ZnO ink onto SiO_2 surface will be the focus for this chapter. ZnO has many applications such as gas sensors [17, 65], acoustic sensors [66, 67], UV photodetector, etc. [29, 30, 68], so achieving printable ZnO nanostructures is ideal. Typically, the aim of inkjet printing of ZnO is to create transparent thin films, however, the films are often non-uniform rough

films with poor crystallinity [69-72]. Many ZnO inks have been experimented with, including zinc acetate/methoxyethanol/ethanolamine mixtures [69, 71], and zinc nitrate/ammonia hydroxide [72, 73], and most of them produce rough [69, 73] and porous films [72].

Furthermore, Z value for aqueous solutions composed of methoxyethanol, ethanolamine, and water can range from 10 to 30 [74-76]. Methoxyethanol has a been shown to have a Z parameter of about 17 [75], and in other work ethanolamine zinc acetate mixtures for doped ZnO has shown a Z parameter around10.1 [76]. The ZnO precursor ink in this work is made of equal parts ethanolamine and zinc acetate (0.3 M) and methoxethanol as described in Section 2.1.4, which means the zinc acetate ink in this work most likely ranges from 10 to 17. A Z parameter greater than 10 means the ink used has high fluidity and results in satellite droplets forming instead of single droplets [63, 74], which can lead to varying printing behavior. Small satellite droplets mean the fluid can result in an irregular film with microporous structure described in Section 2.3.3.

Microporous ZnO films are disadvantageous to most applications due to a low film density and poor crystallinity. However, nanoporous ZnO morphology, with feature size comparable to the Debye length (~20 nm) is ideal for taking advantage of oxygen-induced surface electron-depletion [13, 28], a mechanism described in Section 1.4. The strong electron-depletion effect in nanostructure ZnO can result in reduced dark current by orders of magnitude, allowing for enhanced on/off ratio and photoresponsivity upon UV illumination. Therefore, achieving printed nanoporous ZnO is very desirable for high-performance optoelectronic devices.

4.3 *Printed ZnO Device Performance*

The printed ZnO films described in Section 2.3.3 are compared for performance through testing as a UV photoconductor detectors. The regular ZnO acetate precursor (ZnOPr) and ZnO precursor mixed with ZnO QDs (ZnOPrQDs) discussed in Section 2.1.4 are used to fabricate the films. The incorporation of the highly crystalline ZnO QDs is expected to generate two effects. First, the ZnO QDs of diameter of 5-6 nm could generate a scaffold in the otherwise highly fluidity zinc acetate ink, promoting the nanoporous morphology to form and preventing surface tension driven microporous morphology. On the other hand, the high crystallinity of the ZnO QDs will reduce the growth defects due to crystallization of the zinc acetate. Remarkably, higher photoresponsivity by an order of magnitude has been observed in ZnO UV detectors printed from ZnOPrQDs ink as oppose to that from the reference ZnOPr ink. This large difference in the device performance can be well explained by the difference in the nanoporous morphology in the former, as compared to the microporous one in the latter. Specifically, the printed ZnOPrQDs UV detectors show a responsivity up to 383.6 A/W at 5 V bias, which is comparable to spin-coated precursor for ZnO nanoparticles (0.1 A/W) [68], and other films summarized in Table 1. This result illustrates the viability of the inkjet printing of high-performance ZnO-nanostructure devices. It should be noted that this enhanced photoresponsivity is at the cost of slower photoresponse [77-79], since the surface-electron-depletion effect is associated to the slower surface oxygen adsorption/desorption process as compared to the inter-band photoexcitation in ZnO bulks [13, 28, 80].

The sample morphology and crystallinity of the printed films is discussed in Section 2.3.3, and the goal is to achieve a nanoporous structure which is preferred for more enhanced surface-electron-depletion effect as discussed earlier due to a larger surface-to-volume ratio. This argument is supported by the higher photoresponse observed in the nanoporous ZnOPrQDs film as compared

to the microporous ZnOPr counterpart. Also the incorporated ZnO QDs facilitate uniform nucleation of ZnO crystallites by providing more interfaces between the highly crystalline ZnO QDs and ZnO precursor (Section 2.3.3). The interfaces and different faces of ZnO can provide lower energy nucleation sites for ZnO crystallites [80-82]. In addition, the more uniform and higher concentration of nucleation sites lead to smaller ZnO NPs link interconnected into a favorable nanoporous network. However, ZnO QDs as seeds for growth of larger ZnO NPs may not be the predominant case as most crystallites have isotropic shapes and many show the comparable dimension to that of the ZnO QDs.

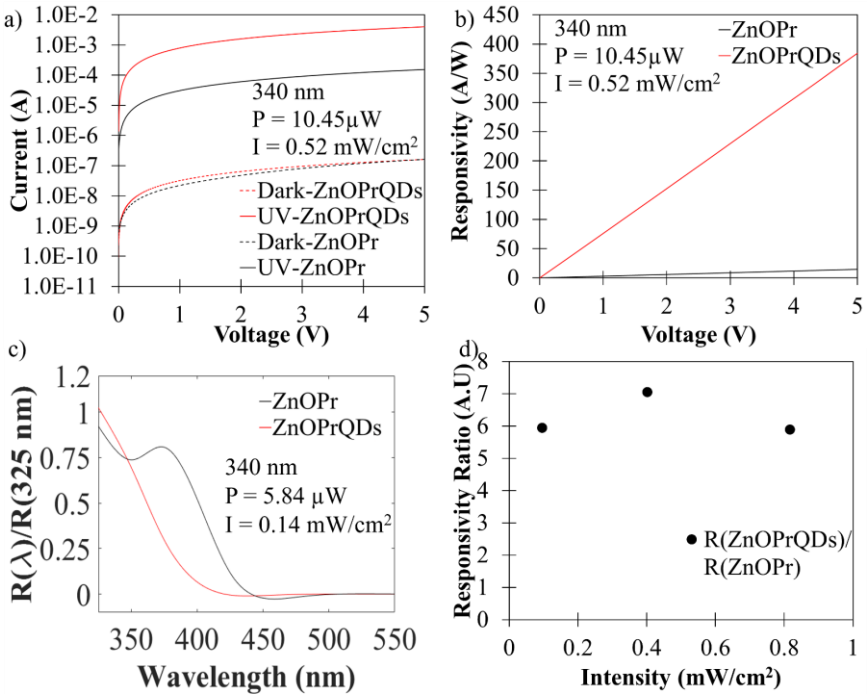

Figure 4.3.1 (a) The dark current and photocurrent of precursor (red) and precursor/QDs (black). (b) Photoresponsivity as a function of voltage bias. (c) The photoresponsivity divided by the photoresponsivity at 325 nm. (d) Responsivity ratio as a function of intensity.

The current-voltage characteristics of the printed ZnOPr and ZnOPrQDs samples were measured in dark and under a monochromatic light source with a wavelength of 340 nm at 0.52

mW/cm^2. The results are compared in Figure 4.3.1 a. The ZnOPr and ZnOPrQDs detectors have similar dark currents while the latter has significantly higher illuminated current. This may be attributed to the nanoporous morphology of the ZnOPrQDs sample for higher surface-to-volume ration and therefore higher electron-depletion effect, as compared to the microporous morphology in the ZnOPrQD sample. The nanoporous and microporous features result in on/off ratio of 2470 in ZnOPrQDs and 949 in ZnOPr samples respectively, and the photoresponsivity at 5 V are 383.6 A/W and 14.7 A/W, respectively (Figure 4.3.1 b). The improved performance by an order of magnitude in the ZnOPrQDs sample as compared to the ZnOPr one illustrates the importance of controlling the morphology and microstructure of the printed ZnO nanostructure UV detectors. The nanoporous structure obtained using ZnO QD-assisted printing from the ZnOPrQDs ink indicates nanocomposite inks by inclusion of QDs may provide a versatile approach towards such control. Figure 4.3.1 c exhibits the responsivity as a function of wavelength measured on both ZnOPrQDs and ZnOPr samples. A band edge around 375 nm is clearly visible for ZnOPr, however ZnOPrQDs show some blue shifted behavior in the band edge, likely caused by nanostructure ZnO QDs. The photoresponsivity ratio as a function of intensity at a 1 V bias is shown in Figure 4.3.1 d, the responsivity ratio shows that ZnOPrQDs stay about 6 times the responsivity of ZnOPr at lower intensities. Notice that the responsivities are not the same for every figure, this is do aging of samples after fabrication, which results in dramatic shifts in dark current after fabrication; however, the ZnOPrQDs maintains better photoresponsivity than ZnOPr counterparts. The stability of the ZnO material will be discussed in the next section.

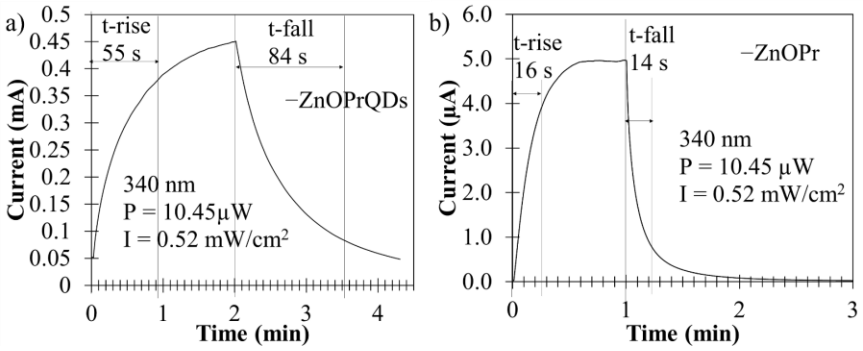

Figure 4.3.2 (a) The ZnOPr has a rise and fall time 16 s and 14 s, and (b) the ZnOPrQDs shows a rise and fall time of 55 s and 84 s respectively, both films were tested at a 5 V bias.

In Figure 4.3.2, the dynamic response shows a rise/fall times of 16 s/14 s for the ZnOPr, and 55 s/84 s for the ZnOPrQDs, respectively. These rise/fall times on the order of few to few tens of seconds because of surface oxygen absorption desorption, and the much longer than bulk ZnO response times [13, 28, 77-80]. Furthermore, the moderately increased response times in the ZnOPrQDs sample may be attributed also to increased grain boundaries which introduce trap states for charges in the nanoporous network of ZnO particles.

4.4 *Inkjet Printing ZnO Quantum Dots on Graphene*

Growing ZnO nanostructures on graphene as discussed in chapter 3 by hydrothermal method is cheap and can be easily scaled up, but it results in a lot of bi-product waste, energy, time, and is not easily integratable with CMOS technology. A more economically viable route is printing of either prefabricated ZnO nanostructure inks or precursor ink on graphene, and in general printing of nanostructures can become easily integrated with CMOS technology. For example, recently the ZnO QDs described in Section 2.1.3 were used to print on the surface of graphene for a UV photosensitive graphene field-effect transistor (GFET) shown in Figure 4.4.1 [41].

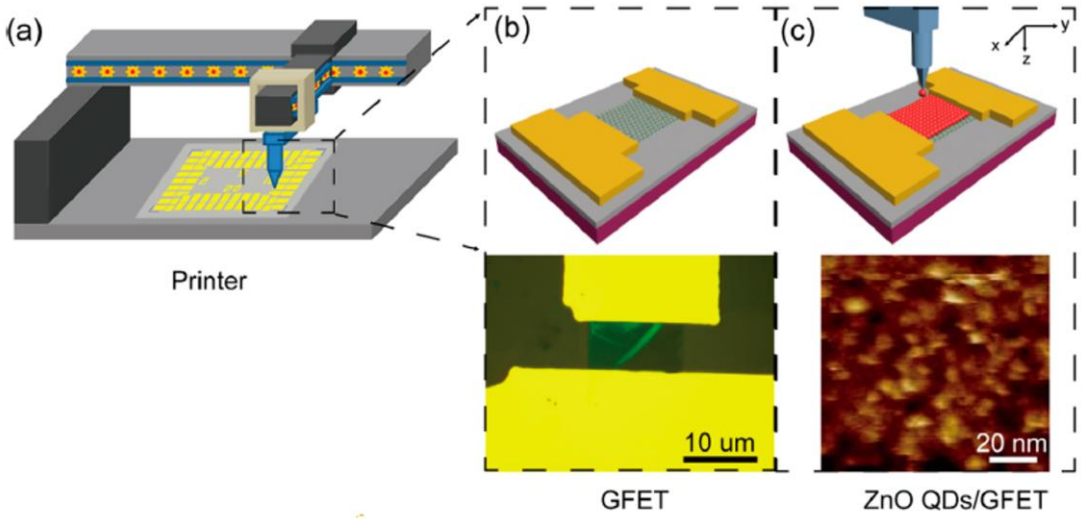

Figure 4.4.1 (a) depicts the printer and (b) and (c) are the before and after printing schematics along with optical image and AFM image as bottom subsets respectively [41]. Adapted from "All-Printable ZnO Quantum Dots/Graphene van der Waals Heterostructures for Ultrasensitive Detection of Ultraviolet Light" by M. Gong et. al., 2017, *ACS Nano*, Vol. 11, pg. 4114-4123, © 2017 American Chemical Society.

The Fermi energy of graphene can be modulated via back-gate voltage and surface dopants as discussed in Section 1.5, and in the case of ZnO QDs, UV light will excite electrons and these electrons will transfer to graphene. The charge transfer between ZnO/graphene interface can be degraded by molecules that coat the surface of ZnO QDs, but with interface modification efficient charge transfer can be achieved which results in a photoresponsivity of up to 9.88×10^{8} A/W [41].

4.5 *Inkjet Printing ZnO Ink on Graphene*

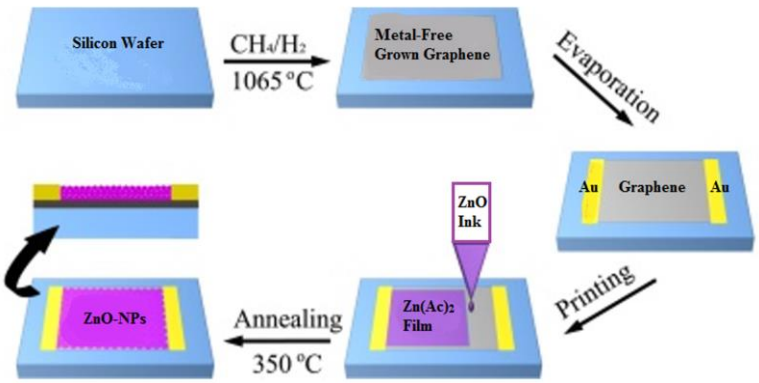

Figure 4.5.1 Process for transfer-free graphene and printed ZnO photoconductor. Adapted from "Transfer-free and printable graphene/ZnO-nanoparticle nanohybrid photodetectors with high performance", by Q. Liu et. al., 2017, *Journal of Materials Chemistry C,* © 2017 The Royal Society of Chemistry, DOI: 10.1039/C7TC01032J.

Further improvements can be made for printed ZnO UV photoconductor by incorporating graphene [83]. Grown CVD graphene on a silicon wafer then gold (Au) electrodes are deposited and finished with printed ZnO ink for ZnO/graphene photodetector (Figure 4.5.1). This process provides a transfer-free process for ZnO/graphene nanohybrids. As discussed earlier (Section 1.5 and Chapter 3) graphene has very high charge mobility and the fermi energy can be easily tuned via surface doping or an applied gate. The large charge mobility in graphene allows for small transit time of the charge carriers between electrodes, as a result the photoconductive gain is greatly increased. In Figure 4.5.2 shows the photovoltaic properties of printed ZnO on graphene. The printed ZnO/graphene photodetector exhibits a has a responsivity an order of magnitude greater (Figure 4.5.2 a) than the printed ZnOPrQDs film alone. Furthermore, the ZnO/graphene photodetector also it exhibits a relatively faster rise and fall times (Figure 4.5.2 b) than the ZnOPrQDs. This process can be repeated for other printable materials on graphene, and allows for mass scalability of graphene on silicon devices.

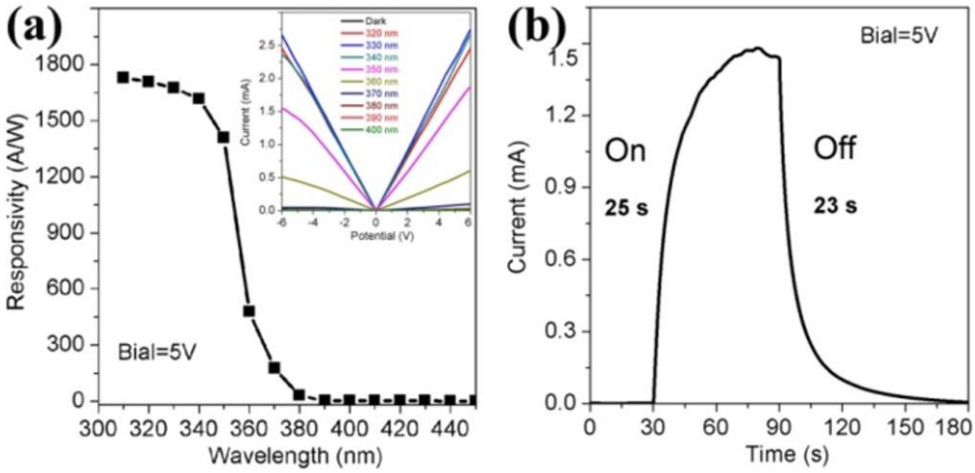

Figure 4.5.2 (a) The responsivity as a function of wavelength, and (b) the dynamic response to 340 nm at 0.1 mW/cm^2 intensity [83]. Adapted from "Transfer-free and printable graphene/ZnO-nanoparticle nanohybrid photodetectors with high performance", by Q. Liu et. al., 2017, Journal of Materials Chemistry C, © 2017 The Royal Society of Chemistry, DOI: 10.1039/C7TC01032J.

4.6 *Stability of ZnO Nanostructures*

Stability of ZnO nanostructures are extremely important for applications of ZnO devices since these devices rely on reproducibility. ZnO is very chemically stable, however, for ZnO nanostructures the surface interactions with the environment can easily influence the performance of the device. Zinc oxide conductivity in general is difficult to control and normally is only n-type, also numerous fabrication choices can result in various interface structures that are a topic of debate [22, 84]. Many efforts are now aimed at modifying the surface of ZnO for optimal performance and stability, for a given application. Many have used surface passivation [85, 86], plasma treatments [87, 88], and environment studies [89-91] to find the best conditions for ZnO to maintain the properties after fabrication. The issues that still remain with zinc oxide nanostructures are doping [92, 93], controllable morphology [25, 58], and stability of ZnO in different

environmental conditions [94, 95]. In particular, environmental condition play an important role for zinc oxide detectors. It has been shown that high levels of humidty and CO_2 can cause degradation of ZnO into zinc hydrocarbon molecules increasing zinc oxide resistance [94, 95]. Furthermore, formation of carbon and hydrogen based groups on the surface greatly influences the performance and contact formation with electrodes which affect response time and photovoltaic properties of zinc oxide detectors do to formation of depletion layers [84, 94, 96]. A common solution to these surface formations has been to passivate the zinc oxide surface with polymers like PVA [85] or ligands [86], which have been shown to increase responsivity and dynamic performance.

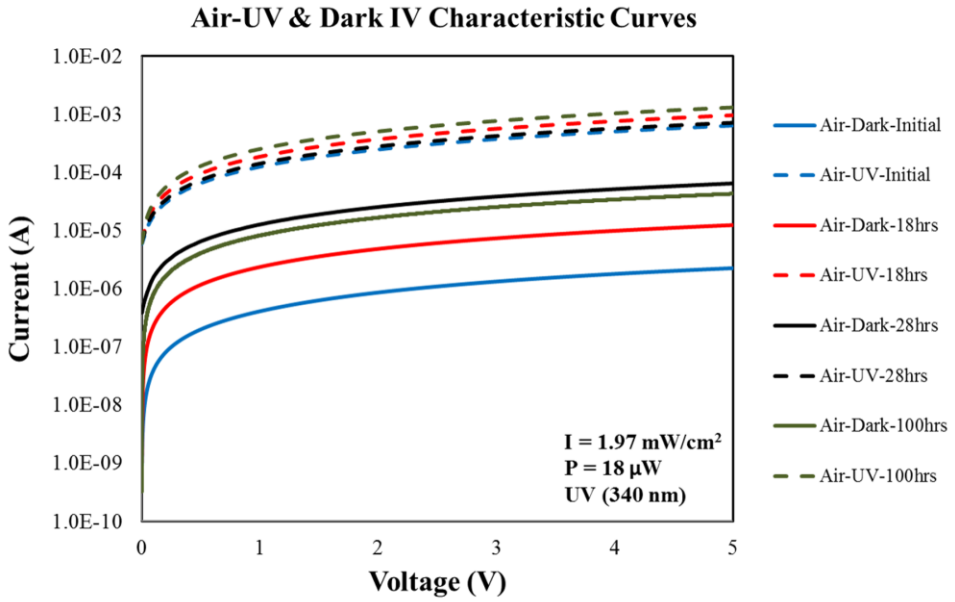

Figure 4.6.1 The current-voltage characteristics of a ZnO film over the course of 100 hours after fabrication.

Zinc oxide thin films fabricated through a precursor spin-coat method described in Section 2.3.3 were investigated under different atmospheric conditions. The stability is observed in air, argon, vacuum, and oxygen, and a mix of argon and oxygen; the voltaic properties are recorded as

function of environment. The critical difference observed over time is a change in dark current and no change in saturation current under UV illumination (Figure 4.6.1), which indicates a source of doping from the atmospheric environment. The ZnO surface has been known to experience the electron-depletion effect which can result in a reduction of carrier density as described in Section 1.4.

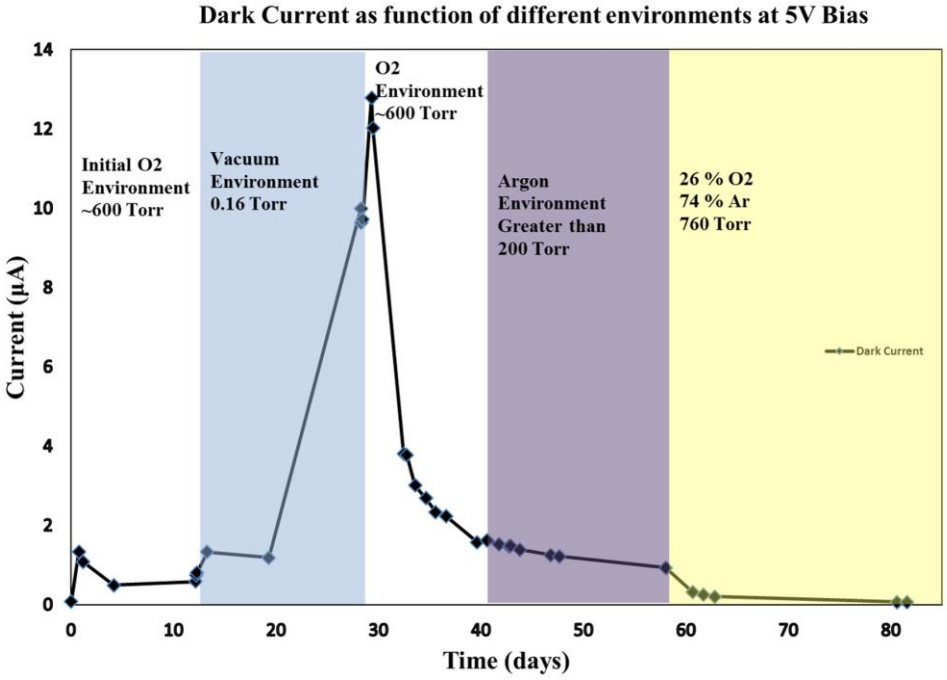

Figure 4.6.2 Dark current as a function of environment and time, the different environment affects how the dark current behaves over time.

To investigate the gas surface effect on ZnO dark current is measured as a function of environment. Oxygen was used to test how much the electron depletion affect changes the dark current and if the dark current can be recovered. In Figure 4.6.2, the initial state of the device of ZnO thin film is placed in a 600 Torr of O_2 gas after being fabricated, over the course of about 12 days the dark current seems to remain relatively constant. The chamber is then vacuumed down to about ~0.16 Torr and after approximately six days the dark current is increased nearly an order of

magnitude, two sources could contribute to the increase of dark current. First, the chamber used in this study is not perfect and could be subject to leaks that may introduce outside air at low chamber pressure, as can be seen in Figure 4.6.1, air will cause a rise in dark current by orders of magnitude. Second, diffusion of oxygen from the ZnO surface do to the differential partial pressure of oxygen with respect to the vacuum, as described earlier desorption of oxygen will return lose electrons to ZnO. Upon, reintroducing O_2 to the chamber at ~600 Torr there is a dramatic reduction of dark current do to oxygen adsorption. Switching the gas to argon results in no change in the dark current trend, this is likely do to some oxygen still in the chamber and diffusing into the ZnO surface. Adding in about 26% oxygen and the rest to argon to about atmospheric pressure causes a small decrease in dark current again, and over the course of 80 days we return to approximately our initial dark current. The large effect of oxygen on ZnO make it a viable gas sensor, and make it difficult to utilize as other types of sensors without complete control over the environment. Consequently, packaging and/or passivating the surface must be heavily considered when make ZnO sensors.

Chapter 5

Conclusions

5.1 *Summary*

Zinc oxide nanostructures have favorable properties for UV detection, such as direct bandgap, large exciton binding energy, and high transparency. Using graphene for its ideal electronic properties in combination with ZnO has led to observed strong p-type doping on graphene, causing graphene to be hole dominant. In addition, strong traps are formed when using seeds to grow ZnO nanowires which results in persist photoconductive behavior and long rise-fall

times of current. In addition, strong p-type doping of graphene from seed layer contributes to negative photocurrent, and poor crystallinity of ZnO and increased trap states at the ZnO/graphene interface. However, the increase density of nanowires forces nanowires to grow perpendicular to surface of substrate, and competition for growth reactants vertically rather than horizontally to substrate limits nanowire diameter growth, resulting in nanowire diameters approaching the nanoscale as opposed to micron scale seen in the seedless graphene surface. This results in more surface and greater sensitivity to oxygen induced electron depletion effect, which results in two orders of magnitude increase in photoresponsivity.

In addition, ZnO precursor (ZnOPr) and ZnO precursor mixed with ZnO quantum dots (ZnOPrQDs) were tested as inks for ultrasonic inkjet printing to observe the effects of photovoltaic performance of printable ZnO ultraviolet photodetectors. Printability was easily achievable but printing had a large variability do to high ink fluidity from large Z parameter values. In addition, the hydrophobicity of SiO_2 results in macroscopic droplets and pores forming from ZnOPr ink. To solve this issue ZnO QDs were implemented to reduce macroscopic pore structures. Both inks show a porous morphology observed under TEM, however a distinguishing difference is ZnOPrQDs have a nanoporous morphology and increased grain boundaries as seen in HRTEM images. The nanoporous morphology in ZnOPrQDs is likely a result from ZnO QDs forming a scaffolding for ZnOPr ink to link together a more complete film. The increased grain boundaries and nanoporous morphology can facilitate increased oxygen absorption and desorption allowing for more oxygen induced electron depletion effect. This resulted in higher photoconductive gain at the cost of longer rise and fall times. Other ZnO nanostructures were also printed on graphene and shows viability as a high performing nanohybrid UV detectors.

References

1. S. E. Thompson, S. Parthasarathy, *Moore's law: the future of Si microelectronics.* Materials Today, 2006. **9**(6): p. 20-25.
2. D. Bera, L. Qian, T.-K. Tseng, P. H. Holloway, *Quantum Dots and Their Multimodal Applications: A Review.* Materials, 2010. **3**(4): p. 2260-2345.
3. V. A. Fonoberov, A. A. Balandin, *ZnO Quantum Dots: Physical Properties and Optoelectronic Applications.* Journal of Nanoelectronics and Optoelectronics, 2006. **1**(1): p. 19-38.
4. Y. Chen, C. L. Zhu, G. Xiao, *Reduced-temperature ethanol sensing characteristics of flower-like ZnO nanorods synthesized by a sonochemical method.* Nanotechnology, 2006. **17**(18): p. 4537-4541.
5. N. Hongsith, E. Wongrat, T. Kerdcharoen, S. Choopun, *Sensor response formula for sensor based on ZnO nanostructures.* Sensors and Actuators B: Chemical, 2010. **144**(1): p. 67-72.
6. A. Kolmakov, M. Moskovits, *Chemical Sensing and Catalysis by One-Dimensional Metal-Oxide Nanostructures.* Annual Review of Materials Research, 2004. **34**(1): p. 151-180.
7. E. Monroy, F. Omnès, F. Calle, *Wide-bandgap semiconductor ultraviolet photodetectors.* Semiconductor Science and Technology, 2003. **18**: p. R33-R51.
8. A. K. Stober, R. Scolnik, J. P. Hennes, *A Vacuum Ultraviolet Photoionization Detector.* Applied Optics 1963. **2**(7): p. 735-740.
9. Z. Xu, B. M. Sadler, *Ultraviolet Communications Potential and State-of-the-Art.* IEEE Communication Magazine 2008. **46**(5): p. 68-73.
10. G. T. Hicks, T. A. Chubb, R. R. Meier, *Observations of Hydrogen Lyman Alpha Emission from Missile Trails.* Naval Research Lab Washington DC, 1976.
11. R. D. McGunigle, H. W. Jackson, R. R. Beavers, *Applicability of Fiber optics to aircraft fire detetion systems.* HTL Industries INC. Santa Anna, CA K. West Div. , 1978.
12. M. Gershenzon, R. O. Engh, P. E. Petersen, *UV Detector materials Development Program.* Honeywell Corporation Technology Center Bloomington, Mn, 1981.
13. J. Zhong, Y. Lu, *ZnO-Based Ultraviolet Detectors*, in *Zinc Oxide Materials for Electronic and Optoelectronic Device Applications*, Cole W. Litton, Donald C. Reynolds, and T.C. Collins, Editors. 2011, John Wiley and Sons Ltd. p. 285-329.
14. Y. A. Goldberg, *Semiconductor near-ultraviolet photoelectronics.* Semiconductor Science and Technology, 1999. **14**: p. R41-R60.
15. Z. Alaie, S. Mohammad Nejad, M. H. Yousefi, *Recent advances in ultraviolet photodetectors.* Materials Science in Semiconductor Processing, 2015. **29**: p. 16-55.
16. Z. L. Wang, J. Song, *Piezoelectic Nanogenerators Based on Zinc Oxide Nanowire Arrays.* Science, 2006. **312**: p. 242-246.
17. Y. V. Kaneti, J. Yue, X. Jiang, A. Yu, *Controllable Synthesis of ZnO Nanoflakes with Exposed (10$\bar{1}$0) for Enhanced Gas Sensing Performance.* The Journal of Physical Chemistry C, 2013. **117**(25): p. 13153-13162.

18. C.-F. Li, C.-Y. Hsu, Y.-Y. Li, *NH3 sensing properties of ZnO thin films prepared via sol–gel method.* Journal of Alloys and Compounds, 2014. **606**: p. 27-31.
19. J. W. Liu, J. Wu, M. Z. Ahmad, W. Wlodarski, *Hybrid Aligned Zinc Oxide Nanowires Array On CVD Graphene for Hydrogen Sensing*, in *Transducers & Eurosensors XXVII: The 17th International Conference on Solid State Sensors, Actuators and Microsystems* 2013, IEEE: Barcelona, Spain p. 194-197.
20. K. Y. Hwa, B. Subramani, *Synthesis of zinc oxide nanoparticles on graphene-carbon nanotube hybrid for glucose biosensor applications.* Biosens Bioelectron, 2014. **62**: p. 127-33.
21. M. Tak, V. Gupta, M. Tomar, *Flower-like ZnO nanostructure based electrochemical DNA biosensor for bacterial meningitis detection.* Biosens Bioelectron, 2014. **59**: p. 200-7.
22. A. Janotti, C. G. Van de Walle, *Fundamentals of zinc oxide as a semiconductor.* Reports on Progress in Physics, 2009. **72**(12): p. 126501-126530.
23. Z. L. Wang, *Zinc oxide nanostructures: growth, properties and applications.* Journal of Physics: Condensed Matter, 2004. **16**(25): p. R829-R858.
24. S. Xu, Z. L. Wang, *One-dimensional ZnO nanostructures: Solution growth and functional properties.* Nano Research, 2011. **4**(11): p. 1013-1098.
25. K. Sambath, M. Saroja, M. Venkatachalam, K. Rajendran, N. Muthukumarasamy, *Morphology controlled synthesis of ZnO nanostructures by varying pH.* Journal of Materials Science: Materials in Electronics, 2011. **23**(2): p. 431-436.
26. S. M. Sze, K. K. Ng, *Physics of Semiconductor Devices*. Third ed. 2007, Hoboken, New Jersey John Wiley & Sons, Inc. .
27. F. H. L. Koppens, T. Mueller, P. Avouris, A. C. Ferrari, M. S. Vitiello, M. Polini, *Photodetectors based on graphene, other two-dimensional materials and hybrid systems.* Nature Nanotechnology, 2014. **9**: p. 780-793.
28. K. Liu, M. Sakurai, M. Aono, *ZnO-based ultraviolet photodetectors.* Sensors (Basel), 2010. **10**(9): p. 8604-8634.
29. Y. Liu, C. R. Gorla, S. Liang, N. Emanetoglu, Y. Lu, H. Shen, M. Wrabrack, *Ultraviolet Detectors Based on Epitaxial ZnO Films Grown by MOCVD.* J. Electron. Mater. , 2000. **29**(1): p. pg. 69-74.
30. Z. Ke, Z. Yang, M. Wang, M. Cao, Z. Sun, J. Shao, *Low temperature annealed ZnO film UV photodetector with fast photoresponse.* Sensors and Actuators A: Physical, 2017. **253**: p. 173-180.
31. M. Li, W. Anderson, N. Chokshi, R. L. DeLeon, G. Tompa, *Laser annealing of laser assisted molecular beam deposited ZnO thin films with application to metal-semiconductor-metal photodetectors.* Journal of Applied Physics, 2006. **100**(5): p. 053106.
32. M. Y. Liu, S. Y. Chou, *Internal emission metal-semiconductor-metal photodetectors on Si and GaAs for 1.3 μm detection.* Applied Physics Letters, 1995. **66**(20): p. 2673-2675.
33. S. Liang, H. Sheng, Y. Liu, Z. Huo, Y. Lu, H. Shen, *ZnO Schottky ultraviolet photodetectors.* Journal of Crystal Growth, 2001. **225**: p. 110-113.
34. C. Kittel, *Introduction to Solid State Physics* 2005, John Wiley & Sons, Inc. .
35. F. Masuoka, K. Ooba, H. Sasaki, H. Endo, S. Chiba, K. Maeda, H. Yoneyama, I. Niikura, Y. Kashiwaba, *Applicability of ZnO single crystals for ultraviolet sensors.* physica status solidi (c), 2006. **3**(4): p. 1238-1241.

36. S. I. Inamdar, K. Y. Rajpure, *High-performance metal–semiconductor–metal UV photodetector based on spray deposited ZnO thin films.* Journal of Alloys and Compounds, 2014. **595**: p. 55-59.
37. A. K. Geim, K. S. Novoselov, *The rise of graphene.* Nature Materials, 2007. **6**: p. 183-191.
38. R. R. Nair, P. Blake, A. N. Grigorenko, K. S. Novoselov, T. J. Booth, T. Stauber, N. M. Peres, A. K. Geim, *Fine structure constant defines visual transparency of graphene.* Science, 2008. **320**(5881): p. 1308.
39. K. S. Novoselov, A. K. Geim, S. V. Morozov, D. Jiang, M. I. Katsnelson, I. V. Grigorieva, S. V. Dubonos, A. A. Firsov, *Two-dimensional gas of massless Dirac fermions in graphene.* Nature, 2005. **438**(7065): p. 197-200.
40. D. Reddy, L. F. Register, G. D. Carpenter, S. K. Banerjee, *Graphene field-effect transistors.* Journal of Physics D: Applied Physics, 2012. **45**(1): p. 019501.
41. M. Gong, Q. Liu, B. Cook, B. Kattel, T. Wang, W. L. Chan, D. Ewing, M. Casper, A. Stramel, J. Z. Wu, *All-Printable ZnO Quantum Dots/Graphene van der Waals Heterostructures for Ultrasensitive Detection of Ultraviolet Light.* ACS Nano, 2017. **11**: p. 4114-4123.
42. W. Guo, S. Xu, Z. Wu, N. Wang, M. M. Loy, S. Du, *Oxygen-assisted charge transfer between ZnO quantum dots and graphene.* Small, 2013. **9**(18): p. 3031-6.
43. B. D. Boruah, D. B. Ferry, A. Mukherjee, A. Misra, *Few-layer graphene/ZnO nanowires based high performance UV photodetector.* Nanotechnology, 2015. **26**(23): p. 235703.
44. B. D. Boruah, A. Mukherjee, S. Sridhar, A. Misra, *Highly Dense ZnO Nanowires Grown on Graphene Foam for Ultraviolet Photodetection.* Acs Applied Materials & Interfaces, 2015. **7**(19): p. 10606-11.
45. V. Q. Dang, T. Q. Trung, D. I. Kim, T. Duy le, B. U. Hwang, D. W. Lee, B. Y. Kim, D. Toan le, N. E. Lee, *Ultrahigh Responsivity in Graphene-ZnO Nanorod Hybrid UV Photodetector.* Small, 2015. **11**(25): p. 3054-3065.
46. J. Liu, R. Lu, G. Xu, J. Wu, P. Thapa, D. Moore, *Development of a Seedless Floating Growth Process in Solution for Synthesis of Crystalline ZnO Micro/Nanowire Arrays on Graphene: Towards High-Performance Nanohybrid Ultraviolet Photodetectors.* Advanced Functional Materials, 2013. **23**(39): p. 4941-4948.
47. Q. Liu, M. Gong, B. Cook, D. Ewing, M. Casper, A. Stramel, J. Wu, *Fused Nanojunctions of Electron-Depleted ZnO Nanoparticles for Extraordinary Performance in Ultraviolet Detection.* Advanced Materials Interfaces, 2017. 10.1002/admi.201601064: p. 1601064.
48. C.-C. Lin, Y.-Y. Li, *Synthesis of ZnO nanowires by thermal decomposition of zinc acetate dihydrate.* Materials Chemistry and Physics, 2009. **113**(1): p. 334-337.
49. A. C. Ferrari, J. C. Meyer, V. Scardaci, C. Casiraghi, M. Lazzeri, F. Mauri, S. Piscanec, D. Jiang, K. S. Novoselov, S. Roth, A. K. Geim, *Raman spectrum of graphene and graphene layers.* Phys Rev Lett, 2006. **97**(18): p. 187401.
50. C. Casiraghi, S. Pisana, K. S. Novoselov, A. K. Geim, A. C. Ferrari, *Raman fingerprint of charged impurities in graphene.* Applied Physics Letters, 2007. **91**(23): p. 233108.
51. A. Das, S. Pisana, B. Chakraborty, S. Piscanec, S. K. Saha, U. V. Waghmare, K. S. Novoselov, H. R. Krishnamurthy, A. K. Geim, A. C. Ferrari, A. K. Sood, *Monitoring dopants by Raman scattering in an electrochemically top-gated graphene transistor.* Nat Nanotechnol, 2008. **3**(4): p. 210-5.

52. W. X. Wang, S. H. Liang, T. Yu, D. H. Li, Y. B. Li, X. F. Han, *The study of interaction between graphene and metals by Raman spectroscopy.* Journal of Applied Physics, 2011. **109**(7): p. 07C501.
53. C. Y. Kao, C. L. Hsin, C. W. Huang, S. Y. Yu, C. W. Wang, P. H. Yeh, W. W. Wu, *High-yield synthesis of ZnO nanowire arrays and their opto-electrical properties.* Nanoscale, 2012. **4**(5): p. 1476-1480.
54. J. X. Wang, X. W. Sun, Y. Yang, H. Huang, Y. C. Lee, O. K. Tan, L. Vayssieres, *Hydrothermally grown oriented ZnO nanorod arrays for gas sensing applications.* Nanotechnology, 2006. **17**(19): p. 4995-4998.
55. J. Yi, J. M. Lee, W. I. Park, *Vertically aligned ZnO nanorods and graphene hybrid architectures for high-sensitive flexible gas sensors.* Sensors and Actuators B: Chemical, 2011. **155**(1): p. 264-269.
56. M. R. Alenezi, S. J. Henley, S. R. Silva, *On-chip fabrication of high performance nanostructured ZnO UV detectors.* Sci Rep, 2015. **5**: p. 8516.
57. Y. Tak, K. Yong, *Controlled Growth of Well-Alligned ZnO Nanorod Array Using a Novel Solution Method.* Journal of Physical Chemistry B, 2005. **109**(41): p. 19263-19269.
58. S. Baruah, J. Dutta, *Hydrothermal growth of ZnO nanostructures.* Science and Technology of Advanced Materials, 2016. **10**(1): p. 013001.
59. L. E. Greene, M. Law, D. H. Tan, M. Montano, J. Goldberger, G. Somorjai, P. Yang, *General Route to Vertical ZnO Nanowire Arrays Using Textured ZnO Seeds.* Nano Letters, 2005. **5**(7): p. 1231-1236.
60. J. B. Shim, H. Chang, S.-O. Kim, *Rapid Hydrothermal Synthesis of Zinc Oxide Nanowires by Annealing Methods on Seed Layers.* Journal of Nanomaterials, 2011. **2011**: p. 1-6.
61. C. Ru, J. Luo, S. Xie, Y. Sun, *A review of non-contact micro- and nano-printing technologies.* Journal of Micromechanics and Microengineering, 2014. **24**(5): p. 053001.
62. G. Pace, A. Grimoldi, M. Sampietro, D. Natali, M. Caironi, *Printed photodetectors.* Semiconductor Science and Technology, 2015. **30**(10): p. 104006.
63. D. Jang, D. Kim, J. Moon, *Influence of Fluid Physical Properties on Ink-Jet Printability.* Langmuir, 2009. **25**: p. Pg. 2629-2635.
64. X. Liu, T.-J. Tarn, F. Huang, J. Fan, *Recent advances in inkjet printing synthesis of functional metal oxides.* Particuology, 2015. **19**: p. 1-13.
65. X. B. Jin, Y. X. Li, Y. Su, Z. Guo, C. P. Gu, J. R. Huang, F. L. Meng, X. J. Huang, M. Q. Li, J. H. Liu, *Porous and single-crystalline ZnO nanobelts: fabrication with annealing precursor nanobelts, and gas-sensing and optoelectronic performance.* Nanotechnology, 2016. **27**(35): p. 355702.
66. A. Marcu, C. Viespe, *Laser-grown ZnO nanowires for room-temperature SAW-sensor applications.* Sensors and Actuators B: Chemical, 2015. **208**: p. 1-6.
67. V. Chivukula, D. Ciplys, M. Shur, P. Dutta, *ZnO nanoparticle surface acoustic wave UV sensor.* Applied Physics Letters, 2010. **96**(23): p. 233512.
68. T. Zhang, J. Yu, Y. Deng, N. Tian, P. Gao, *Fast response ultraviolet photodetectors based on solution-processed ZnO nanocrystals.* Science China Technological Sciences, 2015. **58**(8): p. 1328-1332.
69. J. J. Schneider, R. C. Hoffmann, J. Engstler, O. Soffke, W. Jaegermann, A. Issanin, A. Klyszcz, *A Printed and Flexible Field-Effect Transistor Device with Nanoscale Zinc*

Oxide as Active Semiconductor Material. Advanced Materials, 2008. **20**(18): p. 3383-3387.
70. D. H. Lee, Y. J. Chang, G. S. Herman, C. H. Chang, *A General Route to Printable High-Mobility Transparent Amorphous Oxide Semiconductors.* Advanced Materials, 2007. **19**(6): p. 843-847.
71. D. Kim, Y. Jeong, K. Song, S. K. Park, G. Cao, J. Moon, *Inkjet-printed zinc tin oxide thin-film transistor.* Langmuir, 2009. **25**(18): p. 11149-54.
72. S. Y. Cho, Y. H. Kang, J.-Y. Jung, S. Y. Nam, J. Lim, S. C. Yoon, D. H. Choi, C. Lee, *Novel Zinc Oxide Inks with Zinc Oxide Nanoparticles for Low-Temperature, Solution-Processed Thin-Film Transistors.* Chemistry of Materials, 2012. **24**(18): p. 3517-3524.
73. S. T. Meyers, J. T. Anderson, C. M. Hung, J. Thompson, J. F. Wager, D. A. Keszler, *Aqueous inorganic inks for low-temperature fabrication of ZnO TFTs.* Journal of Chemical American Society, 2008. **130**(51): p. 17603-9.
74. A. Lee, K. Sudau, K. H. Ahn, S. J. Lee, N. Willenbacher, *Optimization of Experimental Parameters to Suppress Nozzle Clogging in Inkjet Printing.* Industrial & Engineering Chemistry Research, 2012. **51**(40): p. 13195-13204.
75. A. Matavz, R. C. Frunza, A. Dmovsek, V. Bobnar, B. Malic, *Inkjet printing of uniform dielectric oxide structures from sol-gel inks by adusting the solvent composition.* J. Mater. Chem. C, 2016. **4**: p. pg. 5634-5641.
76. K. Vernieuwe, J. Feys, D. Cuypers, K. De Buysser, B. Derby, *Ink-Jet Printing of Aqueous Inks for Single-Layer Deposition of Al-Doped ZnO Thin Films.* Journal of the American Ceramic Society, 2016. **99**(4): p. 1353-1359.
77. S. P. Ghosh, K. C. Das, N. Tripathy, G. Bose, D. H. Kim, T. I. Lee, J. M. Myoung, J. P. Kar, *Ultraviolet photodetection characteristics of Zinc oxide thin films and nanostructures.* IOP Conference Series: Materials Science and Engineering, 2016. **115**: p. 012035.
78. M. Liu, H. K. Kim, *Ultraviolet detection with ultrathin ZnO epitaxial films treated with oxygen plasma.* Applied Physics Letters, 2004. **84**(2): p. 173.
79. N. Nasiri, R. Bo, F. Wang, L. Fu, A. Tricoli, *Ultraporous Electron-Depleted ZnO Nanoparticle Networks for Highly Sensitive Portable Visible-Blind UV Photodetectors.* Adv Mater, 2015. **27**(29): p. 4336-43.
80. H. K. Yadav, V. Gupta, *A comparative study of ultraviolet photoconductivity relaxation in zinc oxide (ZnO) thin films deposited by different techniques.* Journal of Applied Physics, 2012. **111**(10): p. 102809.
81. D. H. Zhang, *Fast photoresponse and the related change of crystallite barriers for ZnO films deposited by RF sputtering.* J. Phys. D: Appl. Phys., 1995. **28**: p. pg. 1273-1277.
82. B. Wu, S.-W. Zhuang, C. Chi, Z.-F. Shi, J.-Y. Jiang, X.-W. Chu, X. Dong, W.-C. Li, G.-X. Li, Y.-T. Zhang, B.-L. Zhang, G.-T. Du, *Excellent optical quality versus strong grain boundary effect in a double-layer ZnO structure.* Semiconductor Science and Technology, 2016. **31**(3): p. 035012.
83. Q. Liu, M. Gong, B. Cook, D. Ewing, M. Casper, A. Stramel, J. Wu, *Transfer-free and printable graphene/ZnO-nanoparticle nanohybrid photodetectors with high performance.* J. Mater. Chem. C, 2017. 10.1039/c7tc01032j.
84. C. M. Schleputz, Y. Yang, N. S. Husseini, R. Heinhold, H. S. Kim, M. W. Allen, S. M. Durbin, R. Clarke, *The presence of a (1 x 1) oxygen overlayer on ZnO(0001) surfaces and at Schottky interfaces.* J Phys Condens Matter, 2012. **24**(9): p. 095007.

85. L. Qin, C. Shing, S. Sawyer, P. S. Dutta, *Enhanced ultraviolet sensitivity of zinc oxide nanoparticle photoconductors by surface passivation.* Optical Materials, 2011. **33**(3): p. 359-362.
86. A. Rostami, M. Dolatyari, E. Amini, H. Rasooli, H. Baghban, S. Miri, *Sensitive, fast, solution-processed ultraviolet detectors based on passivated zinc oxide nanorods.* Chemphyschem, 2013. **14**(3): p. 554-9.
87. H. Faber, J. Hirschmann, M. Klaumunzer, B. Braunschweig, W. Peukert, M. Halik, *Impact of oxygen plasma treatment on the device performance of zinc oxide nanoparticle-based thin-film transistors.* Acs Applied Materials & Interfaces, 2012. **4**(3): p. 1693-6.
88. T.-H. Wu, I. C. Cheng, C.-C. Hsu, J.-Z. Chen, *UV photocurrent responses of ZnO and MgZnO/ZnO processed by atmospheric pressure plasma jets.* Journal of Alloys and Compounds, 2015. **628**: p. 68-74.
89. D. Cammi, C. Ronning, *Persistent Photoconductivity in ZnO Nanowires in Different Atmospheres.* Advances in Condensed Matter Physics, 2014. **2014**: p. 1-5.
90. K. Tanaka, G. Blyholder, *Adsorbed Oxygen Species on Zinc Oxide in the Dark and under Illumination.* The Journal of Physical Chemistry, 1978. **76**(22): p. 4.
91. C. G. Van de Walle, *Hydrogen as a Cause of Doping in Zinc Oxide.* Physical Review Letters, 2000. **85**(5): p. 4.
92. C. L. Hsu, S. J. Chang, *Doped ZnO 1D nanostructures: synthesis, properties, and photodetector application.* Small, 2014. **10**(22): p. 4562-85.
93. S. Tüzemen, E. Gür, *Principal issues in producing new ultraviolet light emitters based on transparent semiconductor zinc oxide.* Optical Materials, 2007. **30**(2): p. 292-310.
94. J. Cheng, K. M. Poduska, *Ambient Degradation of ZnO Powders: Does Surface Polarity Matter?* ECS Journal of Solid State Science and Technology, 2014. **3**(5): p. P133-P137.
95. M. A. Yaklin, D. A. Schneider, K. Norman, J. E. Granata, C. L. Staiger, *Impacts of Humidity and Temperature on the Performance of Transparent Conducting Zinc Oxide*. 2010 35th IEEE Photovoltaic Specialists Conference. 10.1109/PVSC.2010.56147162010: IEEE. 4.
96. *Zinc Oxide Materials for Electronic and Optoelectronic Device Applications*. First ed, ed. S.G.I.L. Dr Peter Capper, Southampton, UK, U.o.S. Professor Safa Kasap, Canada, and U.o.S. Professor Arthur Willoughby, UK. 2011: John Wiley & Sons, Ltd.